Optimization of Co-Ni-Mg-Al mixed-oxides CO_2 methanation catalysts with solution combustion synthesis: On the importance of Co incorporation and basicity

Paulina Summa [a,b], Katarzyna Świrk [c], Jithin Gopakumar [c], Bogdan Samojeden [b], Monika Motak [b], Magnus Rønning [c], Wouter Van Beek [d], Patrick Da Costa [a]

[a] Institut Jean Le Rond d'Alembert, CNRS UMR 7190, Sorbonne Université
2 place de la gare de ceinture, 78210 Saint-Cyr-l'Ecole, France;

[b] Faculty of Energy and Fuels, AGH University of Science and Technology,
al. A. Mickiewicza 30, 30-059 Kraków, Poland;

[c] Department of Chemical Engineering, Norwegian University of Science and Technology,
Sem Sælands vei 4, 7491 Trondheim, Norway

[d] Swiss-Norwegian Beamline (SNBL), European Synchrotron Radiation Facility,
71, Avenue des Martyrs, 38043 Grenoble, France

Abstract:

Hydrogenation of CO_2 to methane is a promising prospect for the utilization of carbon dioxide. Ni-Mg-Al mixed oxides have been reported to be effective catalysts for this process. Their promotion with cobalt not only allows to improve nickel reducibility, but also enhances surface basicity, and both electronic and textural properties. Herein, the rapid solution combustion synthesis was used r to optimize the introduction of cobalt to the Ni-Mg-Al oxide matrix. Three synthesis strategies were applied to obtain different morphologies and to study their catalytic performance in CO_2 methanation. A series of characterization techniques (ICP-MS, XRD, low-temperature N_2 sorption, H_2-TPR, CO_2-TPD, TEM, XAS) allowed us to conclude that simultaneous combustion of all of the precursors (Ni, Mg, Al, and Co) led to dissociation of both nickel and cobalt to the support Mg-Al oxides, which resulted in the reduction of catalytic activity and blockage of active centers. Splitting the synthesis into two steps and deposition of cobalt and nickel in a separate step increased the availability of active centers, improved surface properties, and catalytic performance. Furthermore, it led to a decrease in the coordination

number of nickel, probably due to higher contribution of cobalt in the metal crystallites, which resulted in improved catalytic activity. Our findings showed that cobalt addition in the second step, in NiCo-D catalyst, enhanced the CO_2 and H_2 conversions for methane production compared to the other applied synthesis strategies.

Keywords: CO_2 methanation, cobalt, nickel, solution combustion synthesis, spinel

1. Introduction

Considering the latest IPCC report, the forecast of CO_2 emissions to the atmosphere, and the forthcoming climate changes, it is necessary to develop technologies for the utilization of carbon dioxide [1]. According to the 2050 long-term strategy of the European Union, the member states should aim at achieving an economy with net zero greenhouse gas emissions by 2050 [2]. CO_2 hydrogenation to methane reaction, developed by Sabatier at the end of the XIXth century is a promising pathway for the utilization of carbon dioxide (Eq. 1).

$$CO_2 + 4H_2 \leftrightarrow CH_4 + 2H_2O \qquad \Delta H^0_{25}\ [kJ \cdot mol^{-1}] = -165.0 \qquad \text{Eq. 1 [3]}$$

Hydrogenation of CO_2 to methane, known also as CO_2 methanation, is a complex redox reaction. The oxidation state of the carbon atom in the carbon dioxide molecule is related to the high kinetic barrier of the eight-electron shift. Considering this, high reduction potential of the catalytic material is necessary. Furthermore, the synthesis method, the loading of active material, and the choice of the support are important as well [4], to obtain a catalyst with high activity, stability, and selectivity towards methane production. The most suitable for CO_2 methanation are d-block transition metals for which activity of the centers shows the following sequence: Ru>Ir>Rh>Ni>Co>Os>Pt>Fe>Mo>Pd>Ag [5].

The most active catalytic centers are noble metals such as Ru or Rh [6–8].They require low loading on the surface of the catalyst, but due to their very high cost, limited availability and complex utilization, a more common option is the use of nickel [9]. Nickel in comparison to noble metals needs significantly higher concentration on the surface of the catalyst, but its low cost as well as high activity and selectivity allow them to be still considered a very promising alternative to expensive noble metals [10]. Accordingly, many researchers focused their attention on developing a useful method to prepare highly efficient Ni-based catalyst for CO_2 methanation. Well-dispersed nickel supported nanoparticles were found to positively

influence catalytic performance, showing that the right choice of a support is equally important. Futhermore, well-developed specific surface area, optimized number and availability of acidic/basic centers, and strong metal-support interaction play a significant role in the catalytic reaction between CO_2 and H_2 to produce CH_4 [11–13]. Metal oxides with relatively high S_{BET} in the range of 100-200 m^2/g and strong interaction with nickel allow the formation of well-dispersed crystallites, which are resistant towards sintering [14]. The sintering is the most likely cause of the catalysts' deactivation during CO_2 methanation. On the contrary to dry reforming of methane (DRM) catalyst [15,16], deposition of coke on the surface of nickel particles is not common. Under typical CO_2 methanation conditions (i.e., temperature range from 250 to 450 °C, atmospheric pressure, and H_2/CO_2 ratio of 4) coke formation is not thermodynamically favored and its influence on the deactivation of the catalyst is negligible, due to the countinous gasification with hydrogen coming from the gas feed [17].

Hydrotalcites are promising precursors for the synthesis of an effective catalyst for CO_2 methanation. Especially the presence of mixed-oxide support phase where magnesium and aluminum are coexisting in an oxide form is advantageous [12,13,18–20]. Aluminum oxide does have an influence on the development of the specific surface area and prevents Ni particles from sintering. Moreover, it has been reported to be the source of weak Lewis acidic sites, which tend to weaken the C-O bond, facilitating dissociation and formation of the final CO_2 methanation products [21–23]. In turn, magnesium oxide structures are responsible for the surface basicity that is essential for the adsorption of CO_2. Mg-O metal-oxygen pairs with an accessible cation are play an important role in medium-strength basicity, allowing the formation of bidentate carbonates from CO_2. Strong centers originating from basic low-coordination oxygen anions (pure MgO) are attributed to unidentate carbonates [24,25]. Mg sites derived from $MgAl_2O_4$ ternary oxide present on the surface are recognized as weak basic sites [26]. $NiAl_2O_4$ is a source of strong basic centers due to oxygen vacancies which promote the

dissociation of CO_2 to CO [26]. Additionally, in comparison to $MgAl_2O_4$, $NiAl_2O_4$ and $CoAl_2O_4$ are characterized by the presence of a partially occupied d-band. In general, the introduction of cobalt allows to strengthen the basic sites and the shift of desorption temperature to higher temperature regions [11]. $CoAl_2O_4$ is similarly considered as a source of strong surface basicity [27,28].

Promotion with different metals can also positively influence the catalytic performance of nickel-based materials. Cobalt was reported to improve the reducibility of Ni, increase hydrogen uptake, provide additional basic centers on the surface, and function as both an electronic and textural promoter [11,29,30]. However, a major drawback of cobalt addition to a nickel catalyst is its tendency to favor the formation of large nickel crystallites on the surface [31–33]. It is possible to add a promoter as a forth element to the Ni-Mg-Al hydrotalcite. Thermal decomposition of such multielemental precursor leads to the formation of homogeneous mixed-oxides [13,18,34]. Once the material is reduced, the promoter may coexist with nickel inside the crystallites as a solid solution [17]. Mixed-oxides derived from hydrotalcites are typically synthesized by co-precipitation method [35]. An alternative to this commony used technique can be solution combustion synthesis (SCS). The SCS is a rapid and facile method for the preparation of catalysts usually containing several coexisting oxide phases with periclase-like or spinel-like structures [36]. In the case of Ni- and Co-containing materials, the promoter may diffuse to the support phase, coexist with nickel in the active phase, or both.

In this work, we focused our attention on the investigation of highly efficient Ni-based catalyst promoted with colbalt. To the best of our knowledge, a solution combustion method used for the synthesis of nickel catalysts has been scarcely reported for CO_2 methanation [37]. The aim of the current study was to investigate the sequence of cobalt introduction to the Ni-Mg-Al mixed-oxide matrix with the SCS.

2. Materials and methods

2.1 Synthesis strategy

The catalysts were prepared with the reagents: $Ni(NO_3)_2 \cdot 6H_2O$ (Sigma Aldrich, purity 99% for analysis), $Mg(NO_3)_2 \cdot 6H_2O$ (Sigma Aldrich, purity 99% for analysis), $Al(NO_3)_3 \cdot 9H_2O$ (Sigma Aldrich, purity 99% for analysis), $Co(NO_3)_2 \cdot 6H_2O$ (Sigma Aldrich, purity 99% for analysis), and urea (Sigma Aldrich, purity 99% for analysis).The 2M solution containing the desired nitrate precursors and urea was placed in the beaker and left for 1 hour at 50°C under vigorous stirring. Subsequently, the solution was poured into the ceramic vessel and placed in the laboratory furnace preheated to 300 °C. The solution was kept at this temperature for 40 minutes. The synthesis of NiCo-D and CoNi-D catalysts was performed in two different steps. For the former, the first step assumed Mg-Al-Ni oxide matrix preparation, which was subsequently covered with cobalt in the second step. For the latter, the first step is regarded as the synthesis of Mg-Al-Co matrix, covered with nickel in the second step. All the studied samples are compared in Table 1.

The chemical reaction equation for urea-assisted synthesis is expressed by Eq. 2 [38,39].The above stoichiometric urea ratio (φ) of 175% was applied.

$$Me^{v}(NO_3)_v \cdot mH_2O + \frac{5}{3}\varphi CO(NH_2)_2 + \frac{5}{2}\varphi O_2 = MeO_{\frac{2}{v}} + \left(m + \frac{10}{3}\varphi\right)H_2O + \left(\frac{5}{3}\varphi + \frac{v}{2}\right)N_2 + \frac{5}{3}\varphi CO_2 + \frac{5}{2}vO_2 \quad \text{Eq. 2}$$

Table 1. List of the presented samples

	1st step (solution combustion synthesis)	**2nd step (solution combustion synthesis)**
NiCo-S	Synthesis of Mg-Al-Ni-Co mixed oxides	-
NiCo-D	Synthesis of Ni-Mg-Al mixed oxides	Deposition of cobalt on the product from 1st step

CoNi-D	Synthesis of Co-Mg-Al mixed oxides	Deposition of nickel on the product from 1st step

2.2 Physicochemical characterization

The catalysts were characterized by using the following methods: ICP-MS, XRD, low-temperature N_2 sorption, H_2-TPR, CO_2-TPD, TEM, XAS.

Inductively coupled plasma mass spectrometry (ICP-MS) measurement was performed on a Thermofisher Scientific iCAP TQ ICP-MS apparatus. The samples were mineralized in a closed system in concentrated nitric acid with the addition of hydrogen peroxide via microwave-assisted mineralization. Each sample in the as-synthesized form was measured twice. X-ray diffraction (XRD) study was carried out on a Panalytical Empyrean diffractometer for the samples after combustion. The diffractometer working in Bragg-Brentano θ-θ geometry was equipped with Cu Kα (λ = 1.5406 Å) radiation. Data were collected within a 2θ range of 10-90 deg. Ex-situ XRD for the reduced and post-run catalysts was performed at the Swiss-Norwegian beamline (SNBL, BM31) at the European Synchrotron Radiation Facility (ESRF) in Grenoble (France). XRD data were collected with a 2D DEXELA detector using a Si (111) channel-cut monochromator, set at a wavelength of 0.3380 Å. XRD results were averaged for ca. 30 s [40]. The size of the Ni crystallite was calculated based on the Scherrer equation, considering the correction related to the instrument broadening and the shape factor of 0.89 [41].

Low-temperature N_2 sorption measurements were carried out with a Belsorp Mini II (BEL Japan). Prior to the measurement, the samples were outgassed for 2 h at 300 °C. Temperature-programmed reduction (H_2-TPR) and CO_2-temperature-programmed desorption (CO_2-TPD) measurements were performed with the BELCAT-M apparatus, equipped with a thermal conductivity detector (TCD). Before the H_2-TPR measurement, the catalysts were outgassed for 2 h at 100 °C, and then reduced in a flow of 5% H_2 in Ar (50 ml/min) from 100 to 950 °C

with the heating ramp of 10 °C/min. CO_2-TPD was performed on the reduced samples, subsequently after H_2-TPR measurement. Firstly, the catalyst was purged in He, then a mixture of 10%CO_2/He was fed for 1 h to adsorb CO_2 on the catalyst. Thereafter, pure He (50 ml/min) was flowed for 15 min to remove weakly adsorbed carbon dioxide. The temperature range of CO_2-TPD measurements was from 100 to 800°C with a heating rate of 10 °C/min. The desorbed volume of CO_2 was calculated from the area under the TPD curve. The setup was calibrated before measurement with a known amount of CO_2, to precisely determine the area of one pulse registered with the TCD.

Transmission electron microscopy (TEM) measurements performed for the reduced catalysts were carried out with JEM-2010 and JEM-2100Plus (JEOL, Tokyo, Japan) transmission electron microscopes operating at 200 kV. Prior to the measurement, the catalysts were dispersed in ethanol and then transferred onto carbon film-coated TEM copper grids via a drop casting method.

XAS and EXAFS measurements were performed at the Swiss-Norwegian beamlines (SNBL, BM31) at the European Synchrotron Radiation Facility (ESRF) in Grenoble, France. XAS spectra were collected at the Ni K-edge using a Si (111) double crystal monochromator in the transmission mode with continuous scanning between 8200 and 9200 eV and a step size of 0.5 eV.

2.3 Catalytic tests

The catalysts were reduced for 1 h at 900 °C under the flow of 5%H_2/Ar (100 ml/min) before the reaction. Catalytic tests for CO_2 methanation were performed with the use of a fixed tubular bed quartz U-type reactor heated inside a vertical electric furnace. A K-type thermocouple placed directly on the reactor outside the catalytic bed was used for temperature control. The fixed-bed reactor was subjected to the gas mixture CO_2/H_2/Ar in the ratio of 1.5/6/2.5 and total

flow of 100 ml/min. Temperature-programmed surface reaction (TPSR) tests were performed with GHSV of 12 000 h^{-1}. The reaction products and the unconverted reactants (CO_2, CO, CH_4, and H_2) were analyzed with an online micro gas-chromatograph (Varian GC4900) equipped with a thermal conductivity detector (TCD). The temperature range of the catalytic tests was from 250 °C to 450 °C, with the catalyst kept at steady-state operation for 30 min at each temperature, with a heating rate between steps of 10°C/min. The best among the studied catalysts was additionally tested with different GHSV of 24 000 and 48 000 h^{-1}. For those tests, volume of the catalytic bed was reduced to 0.25 and 0.125 cm^3. The stability test was carried out at 300 °C for 30 h, under similar experimental conditions in terms of the mixture and GHSV of 12 000 h^{-1}.

Equilibrium CO_2 conversion and selectivity to CH_4 were calculated with HSC Chemistry 5.0 software.

The conversion of CO_2 and the selectivity to CH_4 were calculated based on Eqs. 3 and 4.

$$CO_2 \text{ conversion } \chi_{CO_2} = \frac{F_{CO_2 inlet} - F_{CO_2 outlet}}{F_{CO_2 inlet}} \quad \text{Eq. 3}$$

$$CH_4 \text{ selectivity } \chi_{CH_4} = \frac{F_{CH_4 outlet}}{F_{CO outlet} + F_{CH_4 outlet}} \quad \text{Eq. 4}$$

3 Physicochemical properties

3.1. Textural properties of cobalt-promoted mixed-oxides

Low-temperature N_2 sorption isotherms for the as-synthesized catalysts are compared in Fig. 1. All the obtained isotherms can be classified as type IV, subtype H1 according to the IUPAC classification. The isotherm of CoNi-D sample- is clearly varying from the remaining catalysts, which suggests a different configuration of surface porosity, i.e., its domination with slit-shaped pores. The isotherms drawn for NiCo-S and NiCo-D suggest the presence of bottle-shaped pores

with a narrow entrance [42,43]. This clearly shows the importance of the sequence of synthesis steps assumed during the preparation of catalysts.

The textural properties of the studied catalysts are presented in Table 2. Similar specific surface area was recorded for all as-synthesized catalysts and only small differences can be observed, i.e., 87 m^2/g for CoNi-D, 99 m^2/g for NiCo-D, and 105 m^2/g for NiCo-S. Total pore and mesopore volumes recognized for NiCo-S and NiCo-D were also comparable, 0.080 and 0.055 cm^3 for the former and 0.075 and 0.057 m^3/g for the latter. CoNi-D showed a slightly larger total pore volume of 0.092 cm^3/g and related volume of mesopores of 0.069 cm^3/g. The same average pore diameter of 3 nm was assigned to NiCo-S and NiCo-D, while CoNi-D showed somewhat increased average pores (ca. 4.2 nm).

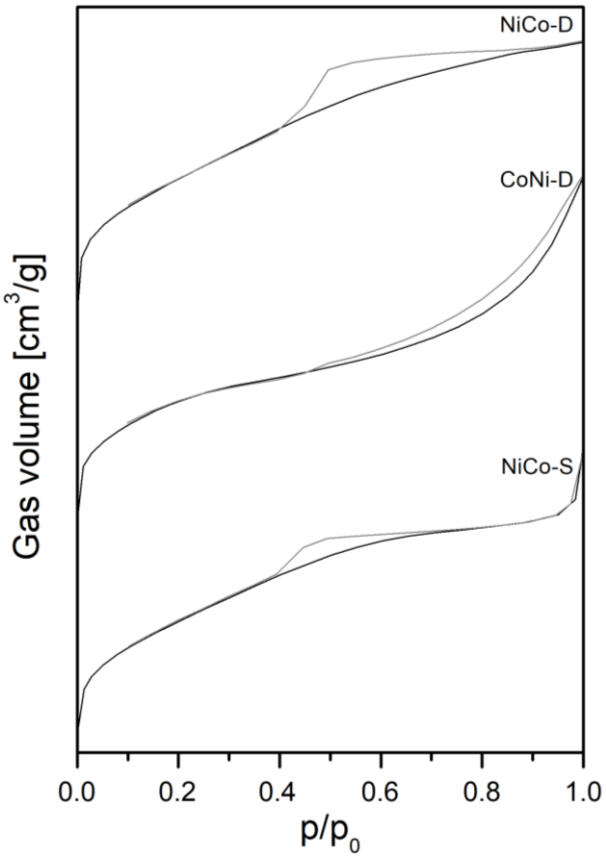

Figure 1. Low-temperature N_2 sorption of cobalt-promoted mixed oxides

Table 2. Specific surface area and porous properties of the SCS-derived cobalt-promoted catalysts

Catalyst	S_{BET} [m^2/g]	Total pore volume [cm^3/g]	d_p [nm]	$V_{mesopores}$ [cm^3/g]
NiCo-S	105	0.080	3.0	0.055
NiCo-D	99	0.075	3.0	0.057
CoNi-D	87	0.092	4.2	0.069

Elemental composition of the studied catalysts obtained from ICP is listed in Table 3. The amount of promoter introduced to the matrix is comparable for all samples, in the range from 1.24 wt% for NiCo-D to 1.56 wt% for CoNi-D. The content of other elements varies, especially between CoNi-D and other catalysts.

For the synthesis of all studied samples, similar (±0.05g) amounts of precursors were used. The registered differences in the mass contribution of each of the detected elements to the overall oxide matrix may be related to the actual type of oxide products formed during solution combustion synthesis. When calculating the synthesis stoichiometry, based on the available literature, it was assumed that each element forms the most feasible oxide form, such as: Ni – NiO, Co – Co_3O_4, Mg – MgO, and Al – Al_2O_3 [44–49]. Possible cross-interactions between metals and their corresponding oxides were not taken into account due to the lack of necessary knowledge about the side interactions. The present study was performed primarily to investigate the influence of cobalt position in the matrix on the performance of Ni-Mg-Al mixed oxide catalysts prepared by the solution combustion synthesis method.

Table 3. Average Ni^0 crystallite size from XRD in the reduced SCS-derived catalysts promoted with Co, based on Scherrer's Equation; the content of Ni, Mg, Al, and Co in the obtained samples, based on ICP results

Catalyst	Average Ni^0 size [nm]	Ni content [wt%]	Mg content [wt%]	Al content [wt%]	Co content [wt%]
NiCo-S	7	19.4	17.9	9.5	1.4
NiCo-D	10	17.0	14.7	8.2	1.2
CoNi-D	8	26.4	20.5	6.7	1.6

3.2 Reducibility of the as-prepared samples

X-ray diffractograms for the cobalt-promoted samples prepared via an alternative sequence of solution combustion synthesis are presented in Fig. 2. The diffractograms clearly differ among the synthesized catalysts both in terms of crystallinity and phase composition. For NiCo-S and NiCo-D, there is a visible shift in the position of the main periclase related peaks at 36.9 deg (111), 42.9 deg (200), 62.3 deg (220), in comparison to the CoNi-D catalyst, suggesting the distortion of the lattice by the Ni atoms present inside the $Mg(Ni,Al)O_x$ crystalline structure [50,51]. This observation was not registered in the CoNi-D sample due to the formation of nickel-free $Mg(Al)O_x$ periclase-like matrix without Ni-related deformations. On the other hand, the beforementioned periclase reflections in CoNi-D sample presented an additional shoulder at the right side of the peak. It may be assigned to the separate NiO phase, formed after the deposition of nickel in the second step of the synthesis. Nickel oxide (ICDD 01-089-7101) is typically characterized by reflections at 2θ with corresponding (00l) planes of 37.2 deg (021), 43.3 deg (202), and 62.9 deg (220). Furthermore, for the CoNi-D sample, sharp peaks were recognized at the reflection characteristic for spinel (probably $MgAl_2O_4$). This kind of ternary oxide in the as-synthesized catalysts was distinguished only for the CoNi-D sample.

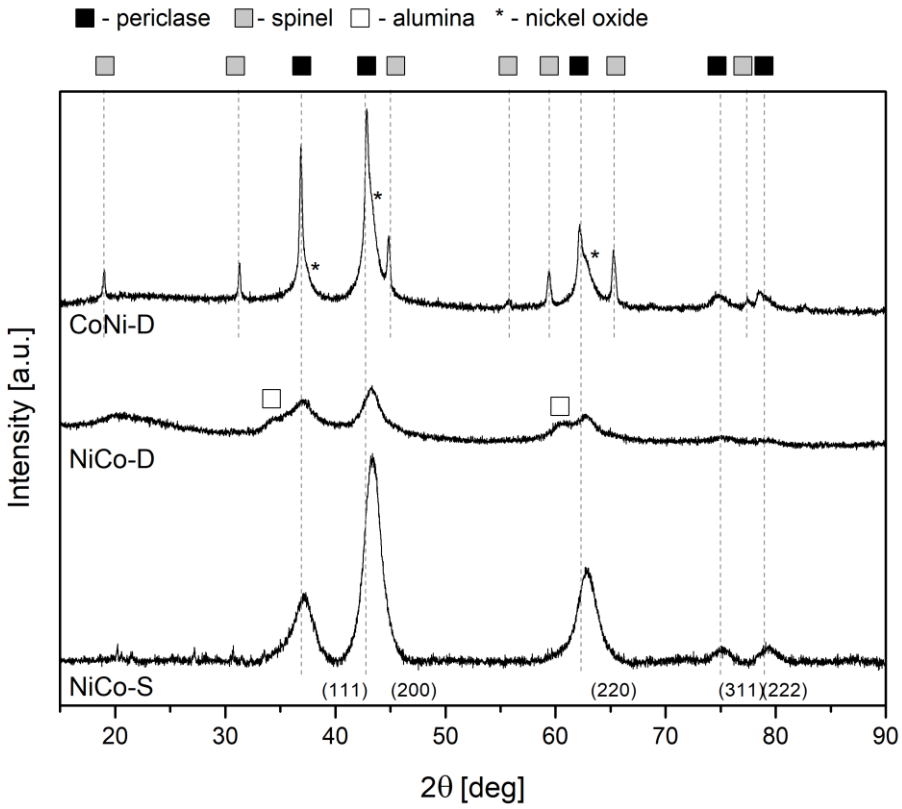

Figure 2. X-ray diffractograms for the as-synthesized cobalt-promoted samples

The NiCo-D catalyst, similarly to the NiCo-S, in which the Ni-Mg-Al oxide matrix was simultaneously synthesized, showed the main reflection characteristic of the periclase-like oxide with a shift towards nickel oxide, discussed above. In the 2θ range below 30 deg, the NiCo-D sample showed low scattering characteristic of the amorphous phase. Additionally, two wide, asymmetric peaks were recognized at 2θ of 35.1 deg and 60.6 deg. They may correspond to the residual phase of AlO_x, probably Al_2O_3 [16,52]. Considering the shape of the reflections, the NiCo-D catalyst is characterized by nanometric crystallites. Large and well-defined crystallites were observed for the CoNi-D catalyst.

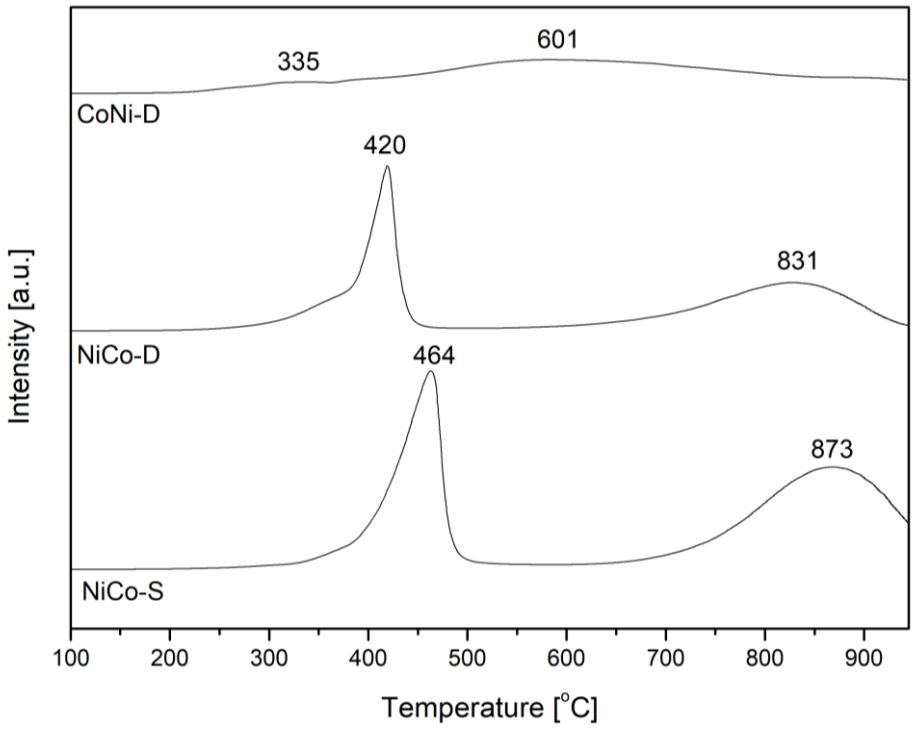

Figure 3. H_2-TPR profiles for the SCS-derived mixed oxides promoted with Co

H_2-TPR profiles for Ni-Mg-Al mixed-oxides promoted with cobalt are compared in Fig. 3. The results recorded for the catalysts in which nickel was simultaneously introduced into the matrix with magnesium and alumina gave comparable profiles. An intense peak was registered with a maximum at 464 °C for NiCo-D and 420 °C for NiCo-S. This peak can be assigned to the reduction of Ni^{2+} to Ni^0 from bulk nickel oxide [53,54]. For those catalysts, the broad peak located at 831 and 873 °C, respectively, is usually assigned to the reduction of Ni^{2+} to Ni^0 in a periclase-like matrix [36]. The sample to which Co was introduced in a separate step resulted in a reduction of the temperature by ca. 40 °C for both types of specimens, in comparison to the catalyst synthesized in the single-step combustion method. These results suggest a different interaction between cobalt and nickel. As reported elsewhere [11,32,55], cobalt facilitates the reduction of nickel by improving the uptake of hydrogen. Similarly, in the case of NiCo-D where Co is expected to be available at the surface, the reduction temperature of Ni was significantly lower, probably due to the facilitated dissociation of hydrogen at the catalyst surface. CoNi-D catalyst reduction profile varied from the former. The intense, explicit peak

typical of the reduction of a single type of sites has not been registered, instead the TPR profile consists of two broad shoulders. The narrower one, located at low temperature with a maximum at 335 °C suggests a continuous reduction of nickel in the first stage from weakly bonded and poorly dispersed crystallites. The broader one with a maximum at 601 °C may correspond to a well-dispersed nickel species with strong metal-support interaction, perhaps partially extracted from a periclase-like matrix. Cobalt co-reduction is possible over the entire temperature range because its position in the matrix is not limited to the support or active phase [11].

3.3 Basicity of the cobalt-promoted mixed-oxides

Temperature-programmed desorption of CO_2 (CO_2-TPD) results for the cobalt-promoted mixed oxides are shown in Fig. 4. The registered profiles were deconvoluted into three Gaussian curves, representing the desorption region of weak (118-145 °C), medium-strength (199-268 °C), and strong (340-436 °C) basic sites. Clearly, higher desorption temperatures were observed for all types of basic centers for the NiCo-D catalyst. In this catalyst, Co was deposited as a separate surface phase. Cobalt has been already reported to increase the desorption temperature in the CO_2-TPD measurements [11]. Considering the aforementioned, it is suggested that for this catalyst the highest amount of cobalt is available on the surface. The CoNi-D sample, in which cobalt was expected to coexist with Mg-Al oxide matrix as a support phase, showed the lowest temperature of the desorption curve for weak basic centers followed by moderate desorption temperatures for medium-strength and strong basic sites. It is evident that the position of cobalt in the matrix does influence the strength of each type of basic centers, mainly through increasing the strength of the interaction between CO_2 on metal-oxygen pairs and low-coordination oxygen anions [11].

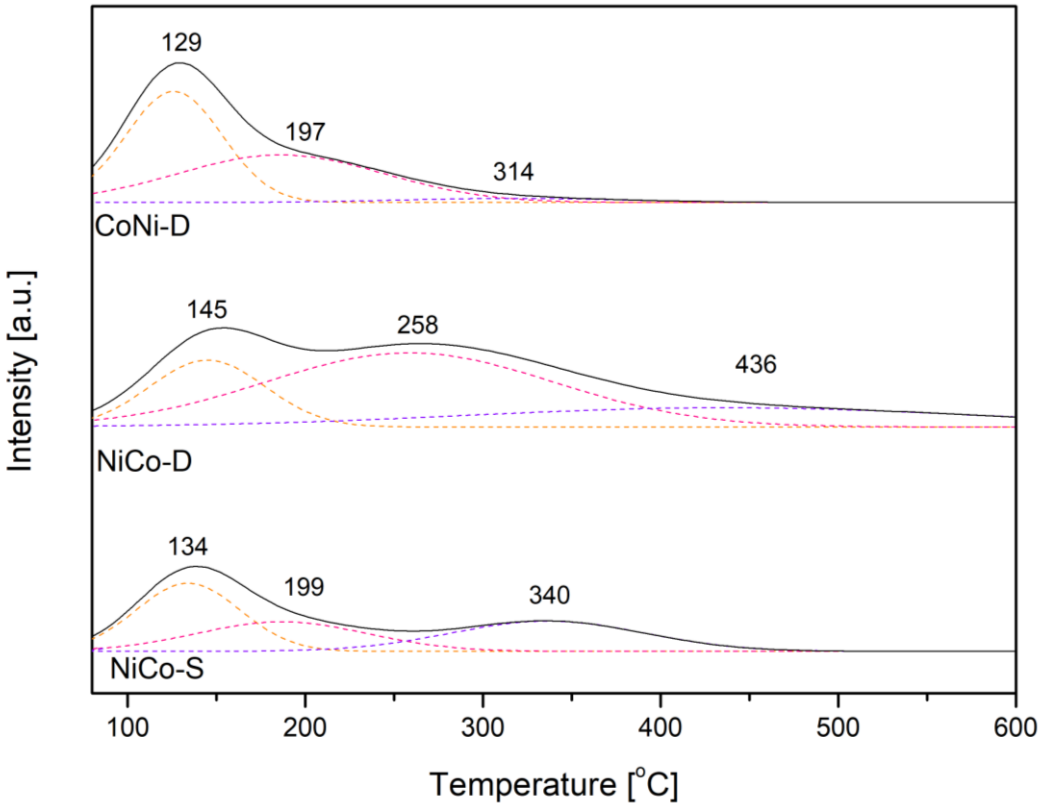

Figure 4. CO_2-TPD profiles for cobalt-promoted Ni-Mg-Al mixed oxides

In Table 4, the distribution of registered basic sites is compared. The total number of basic sites detected in NiCo-D and CoNi-D samples obtained in the two-step combustion is similar, and about two times higher than for the one-step combustion catalyst (NiCo-S). The samples synthesized in the two subsequent steps vary from each other in the predominant type of basicity. The CoNi-D resulted in a very high share of medium-strength basic sites – ca. 95 μmol/g which constituted ca. 57% of the overall share. Furthermore, this catalyst was characterized by a relatively high amount of strong basic sites (ca. 51 μmol/g) and a limited amount of weak centers (ca. 20 μmol/g). On the other hand, the NiCo-D catalyst was dominated with strong basic sites (ca. 74 μmol/g). The content of weak and medium-strength basic centers was comparable (44 and 50 μmol/g respectively). Such strong basicity may be assigned to the improved availability of surface cobalt.

Table 4. Distribution of weak, medium-strength and strong basic sites for the studied catalysts

Sample	Weak [µmol/g]	Medium [µmol/g]	Strong [µmol/g]	Total [µmol/g]	Weak [%]	Medium [%]	Strong [%]
CoNi-D	20	95	51	167	12	57	31
NiCo-D	44	50	74	168	26	30	44
NiCo-S	20	22	34	76	26	29	45

3.4. Evolution of nickel crystalline structure after reduction of Co-Ni-Mg-Al mixed-oxide matrix

The X-ray diffractograms for reduced cobalt-doped samples are compared in Fig. 5. By using the XRD equipped with a channel-cut monochromator of Si (111), it was possible to obtain a better overwview on the crystalline composition, especially considering the expected presence of several types of spinel-like oxides, distinguishable only at high 2θ values. The reported difractograms chracterize highly crystalline catalysts with no scattering from the amorphous phase. The most intense among the distinguished phases is metallic nickel (ICDD 03-065-0380) with reflections at 2θ of 9.53 deg (111), 11.00 deg (020), 15.59 deg (022), 18.29 deg (131), 19.12 deg (222), and 22.11 deg (040). The periclase-like phase (ICDD 00-045-0946) was confirmed with the sharp reflections at 2θ of 7.97 deg (111), 9.21 deg (200), 13.03 deg (220), 15.29 deg (311), 15.98 deg (222), 20.68 deg (420), 22.67 deg (422) which suggests extraction of nickel from the structure during the reduction step. Three spinel-type phases could be observed. First six diffraction lines characteristic for $MgAl_2O_4$ (ICDD 01-070-5187) spinel are overlapping with signal from $CoAl_2O_4$ and $NiAl_2O_4$. The aforementioned peaks are located at 2θ of 4.16 deg (111), 6.79 deg (022), 11.77 deg (242), 12.49 deg (151), 13.60 deg (044), and 15.78 deg (353). Due to the presence of reflections at 2θ 18.47 deg (731), 23.00 deg (931), 23.63 deg (844), 24.97 deg (951) $CoAl_2O_4$ presence (ICDD 00-038-0814) was suggested. The strongest reflections assigned to this phase are typically at 2θ of 7.94 deg (311), 12.64 deg

(511), and 13.58 deg (440), however, they are superimposed with a more intense phase i.e. $MgAl_2O_4$, which is expected to show bigger contribution to the overall matrix.

Similarly, $NiAl_2O_4$ (ICDD 00-010-0339) is recognized with reflections at 2θ of 7.98 deg (311), 12.53 deg (511), 13.64 deg (440), 15.83 deg (533), 18.57 deg (731), 23.75 deg (844), although, those located above 15 deg confirm this kind of ternary structure.

Metallic cobalt (ICDD 00-001-1259) was possible to be separated from nickel considering the reflections above 20 deg. The main three reflections assigned to those metals are at 2θ angles 9.50 deg (111), 15.41 deg (220), and 18.17 deg (311). Additional diffratcion lines at higher 2θ angles assigned in this system to cobalt appeared in the diffractogram (24.08 deg (331), 24.39 deg (420), 28.35 deg). Cobalt-related reflections with low intensity were registered in all samples, although for NiCo-D their signal was higher than for the other catalysts.

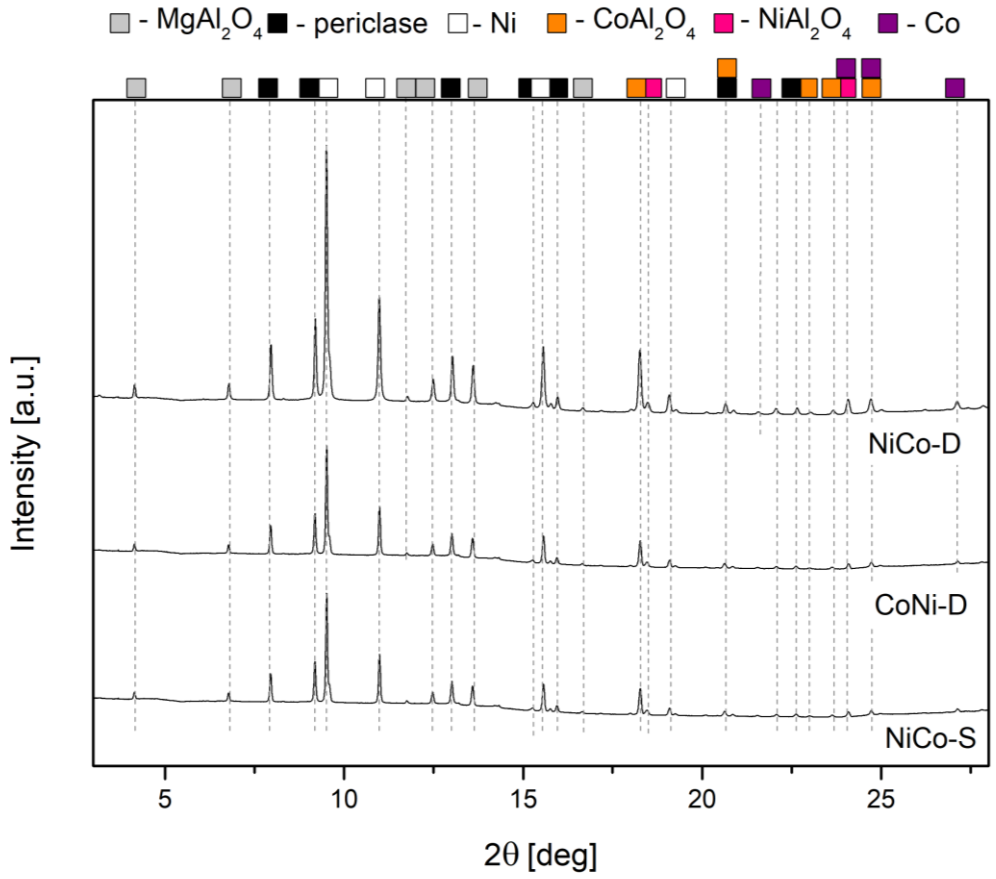

Figure 5. XRD diffractogram of the reduced cobalt-promoted mixed-oxide catalysts

3.5. Morphology of the surface metal particles of mixed-oxide catalysts

Transmission Electron Microscopy was performed to study the distribution of metal particles and the morphology of nickel and cobalt on the surface of the reduced catalyst. TEM images of the reduced cobalt-promoted mixed-oxide catalysts are presented in Fig. 6. 1 (a)-(c) with the corresponding histograms (Fig. 6. 2(a)-(c)). The Ni^0 crystallite size distribution was calculated based on the Rice estimator for the width of the bin [56]. Considering the wide distribution of the metal crystallites, Gaussian curve was drawn for the histograms. The maximum of the curve was used to determine the mean crystallite diameter of the metal particles. The widest particle diameter from ca. 5 to 200 nm was recognized for the CoNi-D catalyst. The average Ni^0 crystallite size of ca. 30 nm was considered as large for the CO_2

methanation catalyst, where usually the goal of the synthesis is to minimize the diameter of nickel particles. It has been reported that large crystallites are prone to coking at high reaction temperatures [57,58]. Additionally, the bigger the diameter of metal crystallites, the lower the dispersion, which limits the availability of catalytically active centers. Thus, with such surface morphology, lowered CO_2 conversion and selectivity to CH_4 could be expected [59].

The NiCo-S catalyst was characterized by the narrowest distribution of metal crystallites among the studied series (diameter range from 13 to 65 nm). Nonetheless, the average Ni^0 particle diameter was comparable to CoNi-D with the value of ca. 31 nm. Intermediate particle distribution was registered for the NiCo-D sample, in the range from 5 to 145 nm. The Ni^0 crystallites smaller than 50 nm dominated on the surface of latter catalyst. The mean diameter of the metal particles is ca. 27 nm, which is the smallest value among the studied series.

The average Ni^0 particle diameter calculated with the Scherrer's equation is clearly smaller than the one estimated by TEM. Two main factors may explain such results: (i) the value obtained on the basis of XRD is averaged for the Ni^0 crystallites present inside the bulk of the studied catalysts and may therefore vary from the TEM results; (ii) as confirmed later by HRTEM, the nickel crystallites were covered with a layer of nickel and cobalt oxides which gave a signal at different 2θ angles than metallic Ni^0, and thus did not affect the reflection parameters of the nickel.

HRTEM images (Fig. 6. 3 (a)-(c)) show the recognized lattice fringe (with its value given in Å). For each of the studied catalysts, several Ni- and Co-containing surface specimens were recognized. Metallic Ni species with (020) plane dominated in all samples [60]. For CoNi-D catalyst, at the edge of the crystallites, species with lattice fringes of 2.44-2.45Å were observed. Commonly, such d-spacing corresponds to spinel oxide, in this case probably $NiAl_2O_4$ or $CoAl_2O_4$ (2.44 Å for (311) plane) [61]. As a result of the exposure of the samples to the atmospheric air, the formation of nickel (II) oxide or hydroxide on the surface of the reduced

Ni^0 crystallites was expected. In this case d-spacing of NiO (111) is 2.41 Å and for $Ni(OH)_2$ (012) 2.60 Å [62,63]. Two more specimens were recognized at the edge of the metal crystallites, with d-spacing of 2.08 and 2.12 Å. Considering the nature of the samples, the former can be assigned to the NiO (200) plane, and the latter to CoO (200) plane [64]. The lattice fringe of 2.17 Å resulted from the (100) plane of Co-Ni alloy [65]. The lowest registered distance of 1.75 Å can be assigned to the Ni (020) plane.

NiCo-S resulted in a similar type of registered lattice fringe parameters. The value of 2.17 Å assigned to the Ni-Co alloy was also observed. The specimens formed during the surface oxidation of nickel crystallites, such as NiO and $Ni(OH)_2$ with the corresponding values of 2.08 and 2.1 Å, and 2.6 Å matching $Ni(OH)_2$ (012) plane. Moreover, Ni (020) plane was dominating with the lattice fringe distance of 1.8 Å. In the obtained images, no planes typical for $NiAl_2O_4$/$CoAl_2O_4$ were detected, which does not exclude the formation of such species in the bulk of the studied materials.

The NiCo-D catalyst, similarly to the former samples, showed lattice fringes corresponding to the plane of metallic nickel (020), oxidized surface specimens such as NiO (200) and CoO (200) (2.08 and 2.13 Å respectively), and formation of the Ni-Co alloy (2.17 Å).

The energy dispersive X-ray (EDX) mapping analysis of the studied catalysts after reduction is shown in Fig. 7. The presence of Ni, Co, Mg, Al, and O elements was demonstrated. In the CoNi-D catalyst, the position of Co is highly correlated with the position of Ni. As confirmed by HRTEM, the negligible content of cobalt was present in the support oxide matrix, suggesting its arrangement mainly in the nickel crystallites, probably as a Ni-Co solid solution. The observed distribution of magnesium and aluminium was uniform throughout the sample. In addition, the presence of oxygen was detected over the places considered metal crystallites, which confirmed the formation of a thin oxide layer on the surface. The EDX mapping of NiCo-

S catalyst showed that cobalt and nickel were partially localized in the metallic crystallites forming an alloy, and dissociated in the oxide matrix of the support. The distribution of Mg in the support was uniform. Aluminum showed an enhanced presence locally, in place of metal crystallites, suggesting that either $NiAl_2O_4$ or $CoAl_2O_4$ is to be expected in those spots. For the NiCo-D sample, as in the case of CoNi-D, cobalt coexists with nickel to form metallic crystallites, but additionally to a certain extent (significantly smaller than in NiCo-S) it was dissociated in the support oxide matrix. The recognized distribution of Mg in the support phase was homogeneous, while Al seemed to agglomerate in some places, suggesting the formation of ternary spinel-type oxides there.

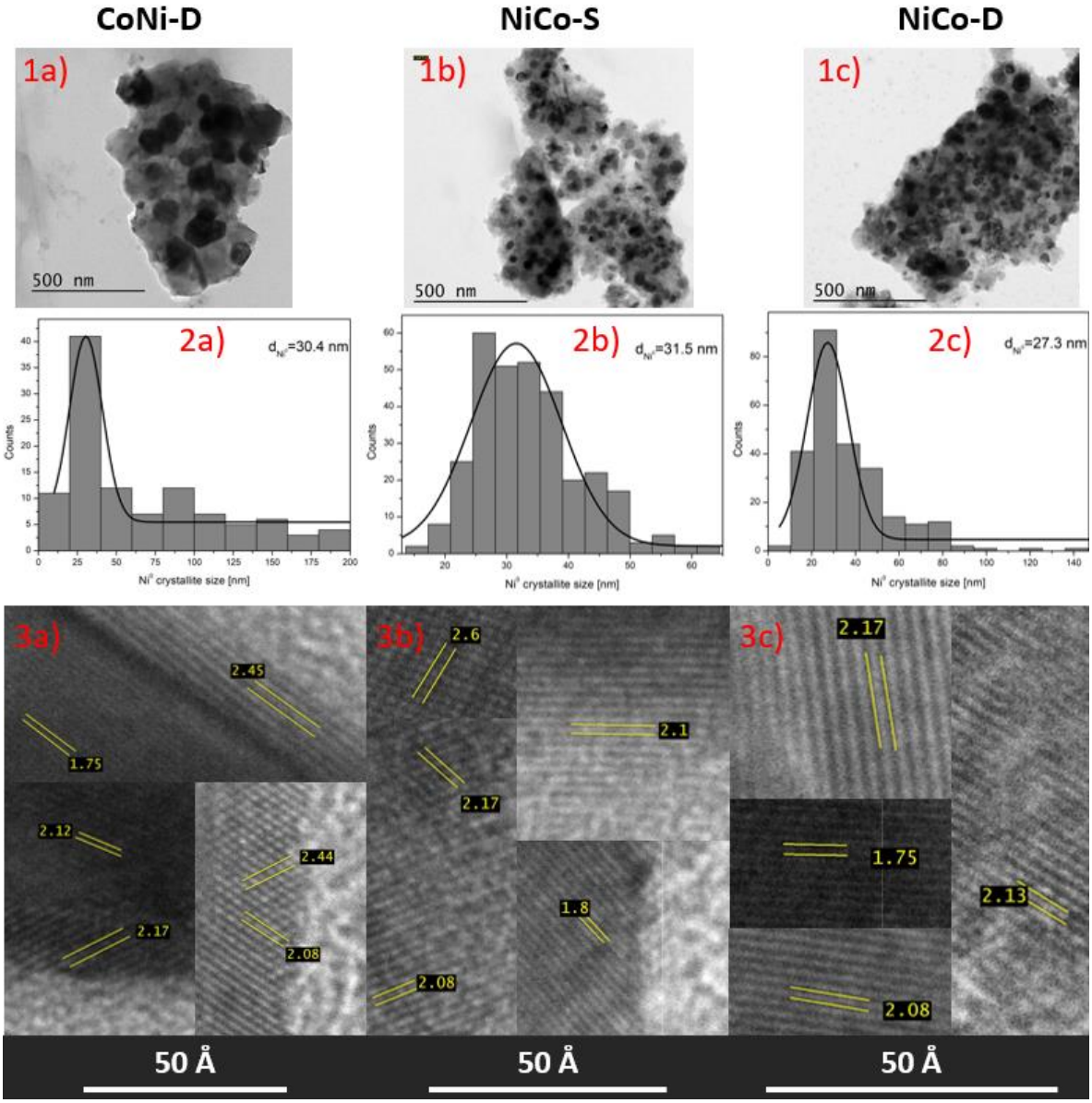

Figure 6. 1(a-c) TEM images of the reduced mixed-oxide catalysts; 2(a-c) histograms corresponding to the studied catalysts in the reduced form; 3(a-c) HRTEM images

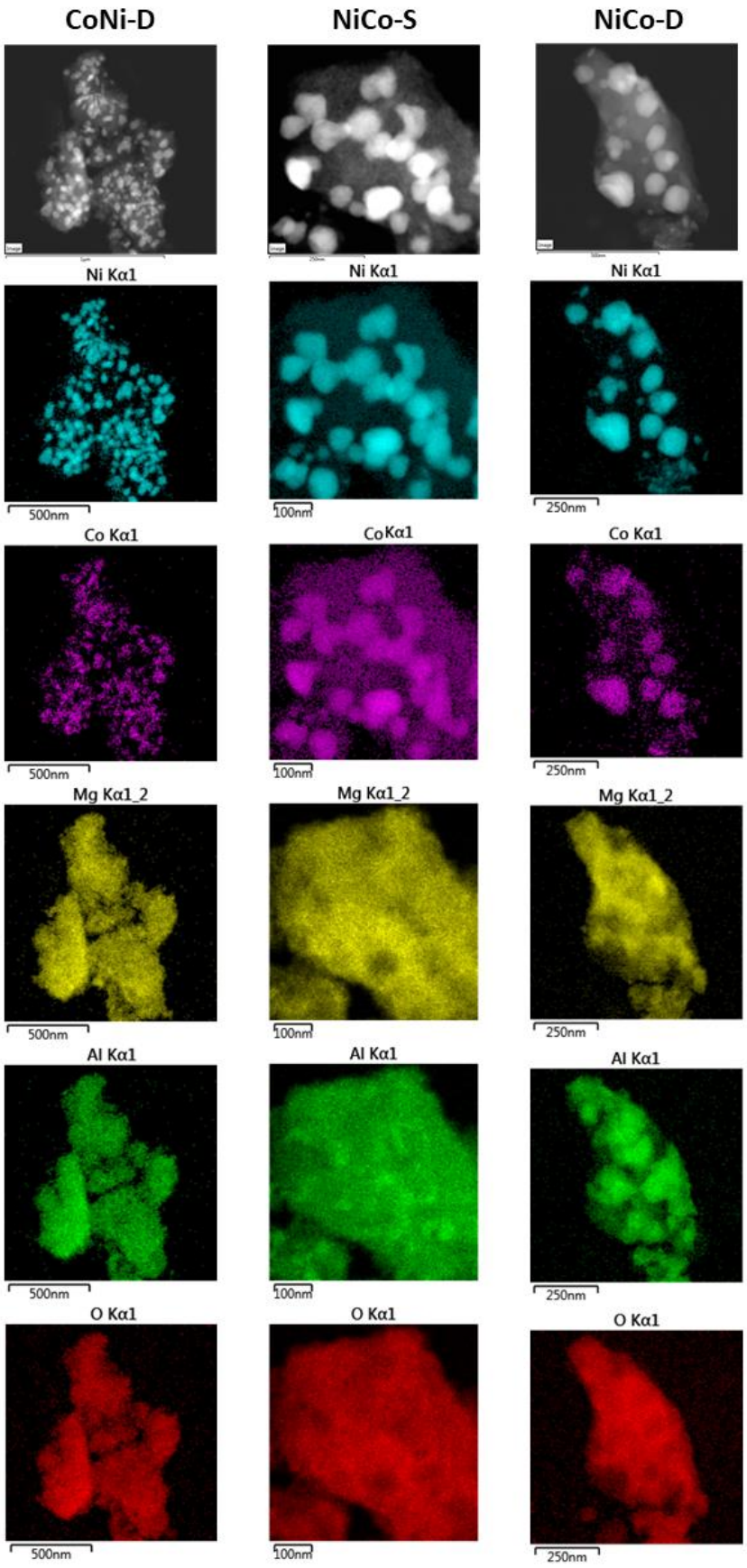

Figure 7. EDX mapping analysis of the reduced cobalt-promoted mixed-oxides

3.6. The effect of synthesis on nickel coordination number in cobalt-promoted Ni-Mg-Al mixed oxides

XANES spectra for the reduced catalysts are presented in Fig. 8 and compared to NiO and Ni foil as a reference. The recorded spectra suggest that nickel exists mainly in its reduced metallic form. Only the NiCo-S catalyst showed partial oxidation of nickel, which is particularly visible in the energy shift registered in the area of the rising edge.

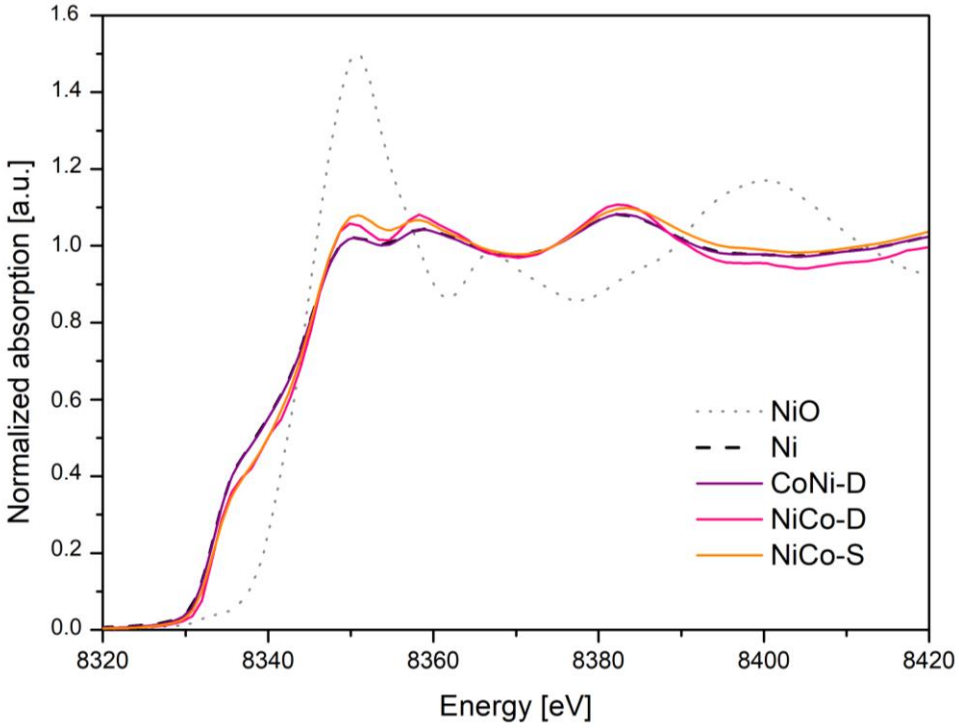

Figure 8. XANES spectra of ex situ reduced catalysts

Considering the EXAFS spectra presented and compared to the metallic nickel standard in Fig. 9, the dominance of the Ni^0 phase is suggested. The first shell was fitted for all the samples and the main parameters are compared in Table 5. The fittings for the second shell and higher were rejected because the fit parameters could not be characterized with a low statistical error. The multiphase composition of the catalysts after reduction resulted in differences in the presented parameters. Considering the XRD results and HRTEM images, expected types of nickel-related

bonds are Ni-Ni (2.479 Å), Ni-O from NiO (2.100 Å), Ni-O from $NiAl_2O_4$ (2.040 Å and 2.070 Å). Co-Co bond is usually characterized with the length of 2.498 Å.

The most accurate fit was obtained for NiCo-D sample. The bond between nickel and nickel(cobalt) was characterized with a coordination number of 9.2, which is lower than for the NiCo-S (9.8), and higher than for CoNi-D (8.7). The former may be characterized by a higher contribution of Ni-Co phase, suggested not only by the higher coordination number, but also a shift in radial distance in the direction of Ni-Co bonding. NiCo-S was also characterized with the largest value of R. CoNi-D showed the lowest radial distance value, suggesting a smaller content of cobalt coexisting within the nickel phase.

Table 5. Coordination number (CN), Radial Distance (R), Debye−Waller Factors (σ), and R-Factor Determined by EXAFS fitting of the Ni K-Edge of the reduced mixed-oxide catalyst promoted with cobalt

NiCo-S				
Path	**CN**	**R (Å)**	**σ^2 (Å^2)**	**R-factor (10^{-2})**
Ni-Me*	9.8 ± 0.7	2.488 ± 0.01	0.0074 ± 0.0006	0.8
Ni-O	0.5 ± 0.1	2.050 ± 0.01	0.0115 ± 0.004	
NiCo-D				
Path	**CN**	**R**	**σ^2**	**R-factor (10^{-2})**
Ni-Me*	9.2±0.5	2.486 ± 0.01	0.0076 ± 0.0004	0.3
Ni-O	0.3±0.1	2.055 ± 0.02	0.0027 ± 0.0008	
CoNi-D				
Path	**CN**	**R**	**σ^2**	**R-factor (10^{-2})**
Ni-Me*	8.7 ± 0.5	2.483 ± 0.02	0.0069 ± 0.0005	0.3

* where Me is Ni or Co

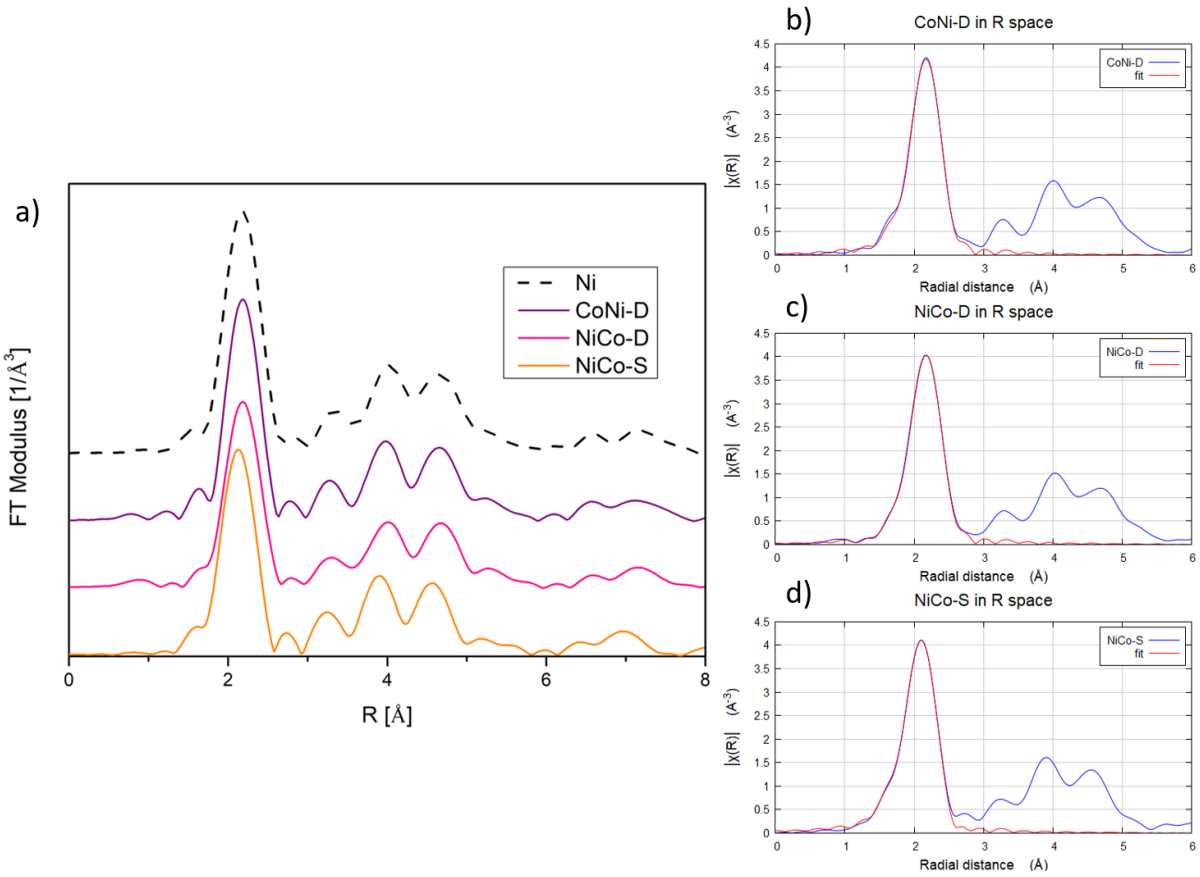

Figure 9. EXAFS results of the studied samples after reduction

4. Catalytic tests

4.1 TPSR tests

The results of TPSR catalytic tests performed on the Ni-Mg-Al mixed oxide samples promoted with cobalt are compared in Fig. 10. At the initial test temperature (250 °C), the samples did not show high catalytic activity. However, NiCo-D catalyst improved the CO_2 conversion by 10% in comparison to the other catalysts. All the presented samples showed an evident increase in activity at the temperature of 300 °C. Under these conditions, the most effective NiCo-D catalyst resulted in 88% of CO_2 conversion, followed by CoNi-D (83%), and NiCo-S (72%). At 350 °C, the studied samples showed similar catalytic activity, from 84% (NiCo-S) to 90% (NiCo-D). At temperatures of 400 °C and above, all cobalt-promoted catalysts reached the CO_2 conversion close to the thermodynamic equilibrium.

The selectivity of the studied samples is presented in Fig. 10 (b). Due to the low activity at the initial test temperature (250 °C), the catalysts did not show total selectivity towards the formation of CH_4. From 300 °C, NiCo-D catalyst was considered the most active among the studied samples, and obtained selectivity to methane was at the thermodynamic equilibrium. The other two samples, NiCo-S and CoNi-D, were also very selective to CH_4, although their performance was slightly (ca. 1-2%) worse than that of the latter catalyst.

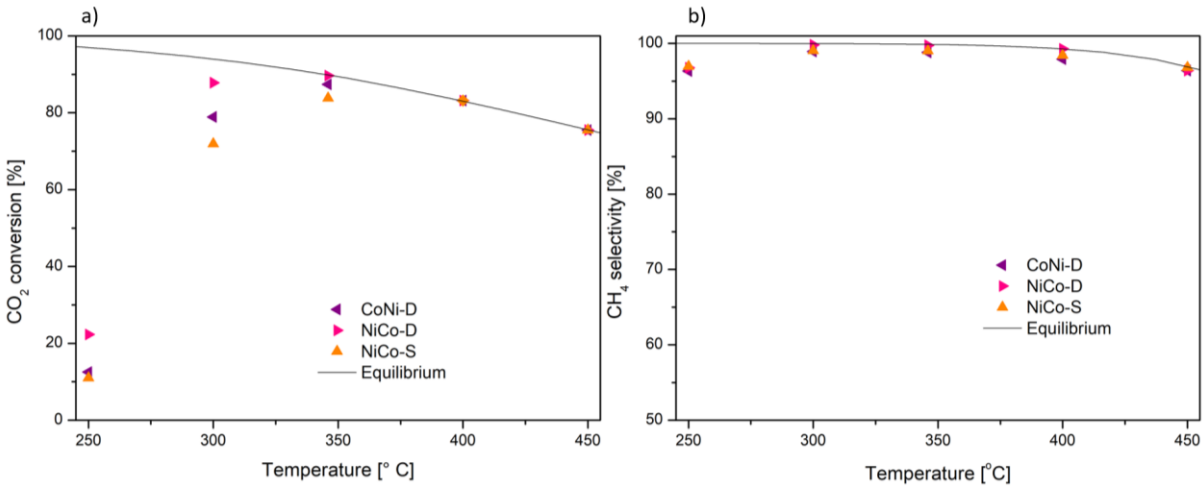

Figure 10. (a) CO_2 conversion and (b) selectivity to CH_4 of the Ni-Mg-Al mixed oxide catalysts promoted with cobalt

4.2 On the influence of GHSV

To study the influence of different gas hourly space velocities (GHSV) on the results of the catalytic tests, additional tests with increased GHSV of 24,000 h^{-1} and 48,000 h^{-1} were carried out on the NiCo-D sample. The results are reported in Fig. 11. At GHSV of 24,000 h^{-1}, the observed catalytic activity is significantly higher (CO_2 conversion of 60%) than at 12,000 and 48,000 h^{-1} (22 and 0% respectively) at the initial test temperature. Such improvement may be assigned to the lowered mass transfer limitations of the gases diffusing through the catalytic bed, due to its smaller size (0.25 cm^3). On the other hand, at the highest studied GHSV of 48,000

h^{-1}, the bed might have been too short (0.125 cm^3) to provide sufficient contact time between the reacting gas mixture and the catalyst which originated in the lack of catalytic activity.

At the elevated temperature range of 300 °C to 450°C, the performance of NiCo-D catalyst at GHSV of 12,000 and 24,000 h^{-1} is comparable. With the highest GHSV of 48,000 h^{-1}, the sample activity is still satisfactory, reaching 72% of CO_2 conversion at 300 °C and increasing to 79 and 80% at 350 and 400 °C, respectively. It was only at 450 °C that the catalyst reached the thermodynamic equilibrium of CO_2 conversion at the GHSV of 48,000 h^{-1}.

Selectivity towards methane formation reached the thermodynamic equilibrium for tests at GHSV of 12,000 and 24,000 h^{-1} at the temperatures from 300 to 450 °C. At 250 °C, the results varied, which can be interpreted as the consequence of the low activity at the initial test temperature, except for the test at 24,000 h^{-1}. For the test at 48,000 h^{-1}, the measured selectivity is very high at temperatures from 300 to 400 °C, equal to 98%, later decreasing to 96% due to the thermodynamic limitations.

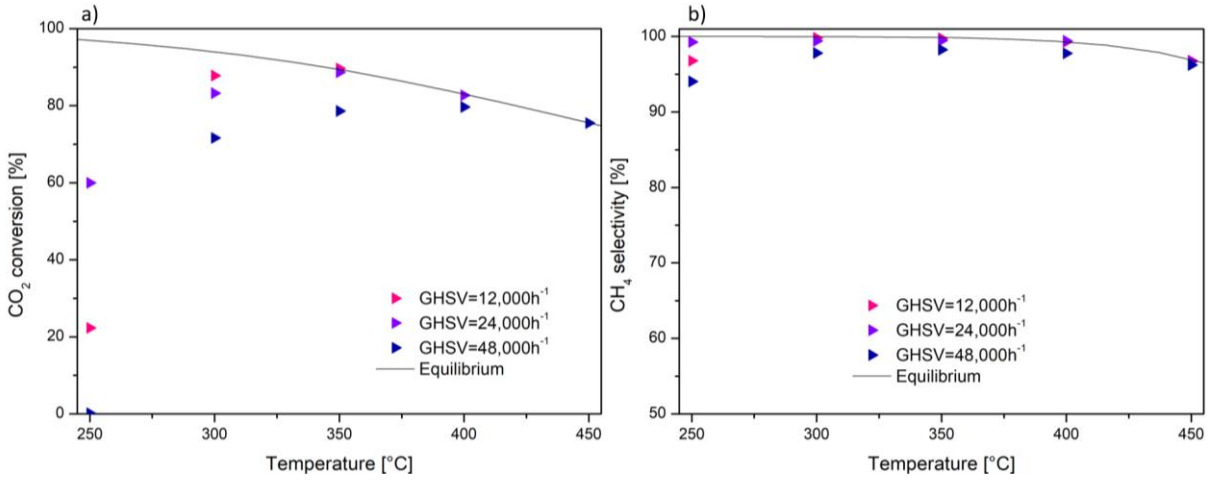

Figure 11. (a) CO_2 conversion and (b) selectivity to CH_4 for NiCo-D catalyst at GHSV of 12,000; 24,000; 48,000 h^{-1} in the TPSR test

The catalytic activity of the presented catalysts can be easily corelated with their physicochemical properties. Indeed, NiCo-D sample presented the highest CO_2 conversion at

300 °C for CO_2 methanation. It was characterized with the smallest size of nickel crystallites (according to TEM) and the highest number of strong basic sites (74 μmol/g). On the other hand, in case of surface basicity, both catalysts synthesized with a two-step synthesis (CoNi-D and NiCo-D) showed almost identical total basicity (167-168 μmol/g). The CoNi-D sample was dominated with medium-strength basic centers (95 μmol/g), which in this study were of secondary value. Considering the similarity of the specific surface area of the studied materials, this factor can be excluded from the further discussion.

The neighborhood of nickel atoms is an additional factor that influences the catalytic performance. The coordination number of the NiCo-D catalyst of 9.2 was moderate, compared to other samples. Additionally, the intensity of crystalline nickel phase diffraction lines in XRD and likewise the significantly stronger signal of $CoAl_2O_4$ spinel oxide were recognized for this catalyst. Referring to the EDX TEM mapping, it is visible that most of cobalt phase coexists with nickel in metal crystallites, however, partially it is also dissociated to support matrix, probably in the $CoAl_2O_4$ spinel form, reported to be the source of strong basic sites. As a result of the partially occupied d-band, spinel-derived centers are responsible for the adsorption and further dissociation of carbon dioxide [11,27]. The catalyst by the lowest activity, NiCo-S, was characterized with the highest coordination number of nickel, and visible dissociation of significant amounts of Ni and Co to the support matrix. It is likely that, as a result of such phenomenon, the sites available on the surface were limited, in comparison to those of the other catalysts, prepared with two-step synthesis. Additionally, a higher coordination number suggests lower content of cobalt coordinated with nickel.

4.3 Stability test

By using the same GHSV, a 26 hour stability test at 300 °C was performed on NiCo-D catalyst which appeared to be the best among the studied samples. During the entire time on the stream,

CO_2 conversion remained constant at the level of 88%, similar to the activity registered in the TPSR test. Simultaneously, the selectivity towards methane formation was found to be higher than 99% for the first 16 hours of test. Negligible fluctuations (ca. 1-1.5%) were registered after that time. The overall test suggests satisfactory stability of both CO_2 conversion and CH_4 selectivity, with no visible premises of deactivation.

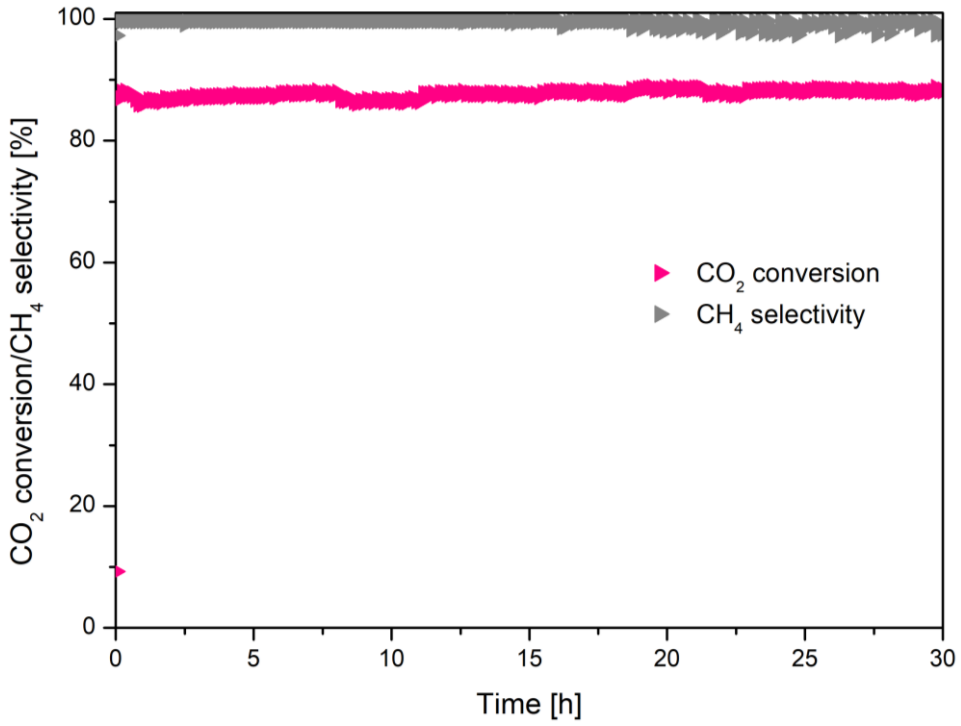

Figure 12. CO_2 conversion and selectivity to CH_4 during the 26h stability test at 300 °C and GHSV of 12,000 h^{-1}

5. Post-run characterization

To investigate possible changes in the composition of the crystalline phase, the XRD was performed on the post-run samples. The diffractograms with corresponding crystallite size calculated from the Scherrer's equation are presented in Fig. 13. Similarly to the reduced catalysts, six phases were identified, such as three spinel-type ternary oxides $MgAl_2O_4$ (ICDD 01-070-5187), $NiAl_2O_4$ (ICDD 00-010-0339), and $CoAl_2O_4$ (ICDD 00-038-0814), periclase-like oxide (ICDD 00-045-0946), and two metallic phases of nickel (ICDD 03-065-0380) and cobalt (ICDD 00-001-1259). The intensity of the signal corresponding to all the types of spinel-

like species decreased after the catalytic test. The most explicit and intense reflections among the registered phases are those originating from metallic nickel. As reported elsewhere [45], this phenomenon may be associated with the weak stabilization of nickel inside the support-oxide matrix, which may result in its migration and sintering [46].

The scattering related to the presence of any amorphous phase was not observed, similarly to the reflections corresponding to the possible formation of crystalline carbon deposits. Taking into account the resolution and sensitivity of the recorded diffractograms, the formation of the latter species can be omitted due to their absence or presence in a negligible amount.

An increase in the average nickel crystallite diameter was observed for all the samples after the catalytic test. Especially, Ni^0 crystallite size increased for the NiCo-S catalyst (from 7 to 17 nm). Thus, promotion with cobalt may lead to increased Ni^0 sintering.

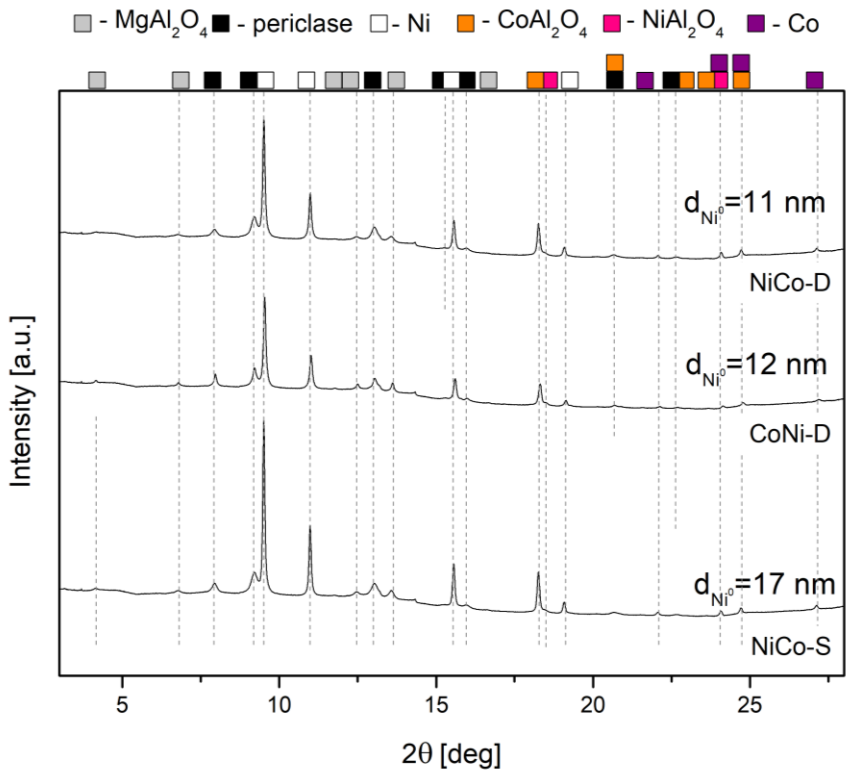

Figure 13. XRD of the cobalt-promoted mixed oxide catalysts after the catalytic test

XANES for the post-run catalysts is presented in Fig. 14. XANES spectra of the catalysts NiCo-D and NiCo-S are comparable to the ones collected for the reduced catalysts, suggesting the presence of nickel mainly in its reduced form. Sample CoNi-D is clearly different, an explicit shift is observed in the rising edge region towards to the direction of nickel oxide. This latter result may be assigned to the partial oxidation of this catalyst during the time-on-stream.

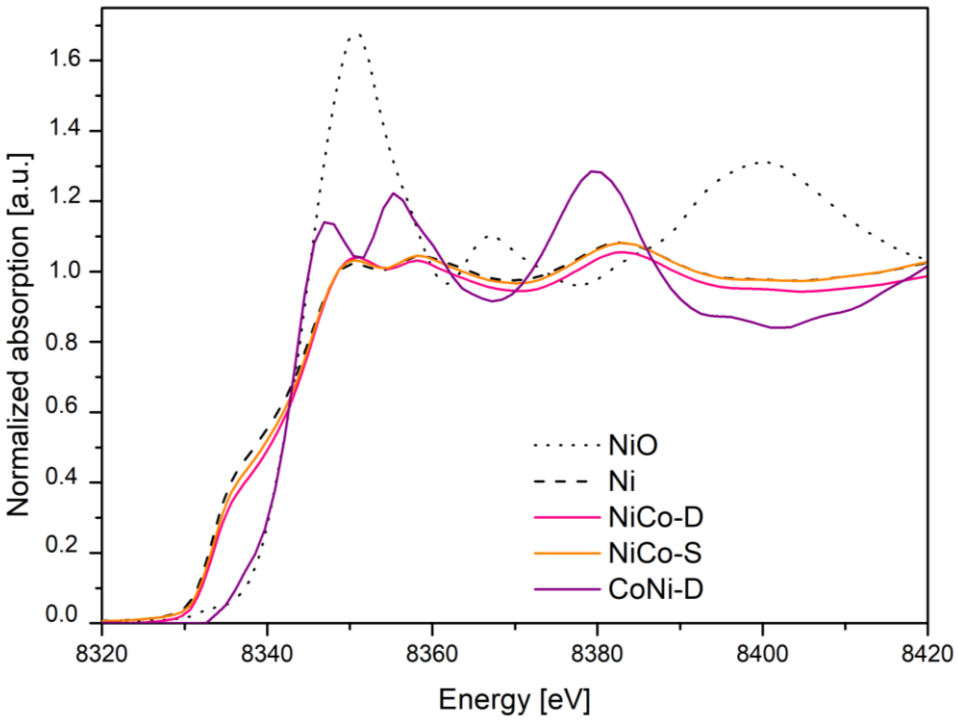

Figure 14. XANES spectra for the post-run catalysts

EXAFS spectra are compared in Fig. 15 and the corresponding fitting parameters are listed in Table 6. The increase in the Ni-Me coordination number of NiCo-S and NiCo-D suggests a higher contribution of Ni-Ni bonds. This is even more pronounced in the NiCo-S sample, where the first shell interatomic distance reached 2.479 Å, which corresponds to the value of the Ni^0 bond. Indeed, the cobalt could be extracted from the Ni-Co solid solution to form a separate phase, i.e., $CoAl_2O_4$. This was confirmed by XRD of the post-run catalysts (Figure 13). On the other hand, considering the severe sintering on NiCo-S catalyst, the contribution of Co could have decreased due to the migration of nickel weakly interacting with the surface, and its agglomeration with the existing crystallites. Larger Ni particles are characterized with higher

coordination number, ca. 12, and the higher observed CN for the NiCo-S catalyst is likewise associated with the increase in the Ni^0 crystallite size [66,67]. For CoNi-D, the coordination number of metal-metal interaction remained comparable to that of the reduced catalyst. Then, it was possible to fit Ni-O interaction to all the presented samples. Furthermore, the decreasing of the length of Ni-O bond suggests a decrease in the contribution of nickel oxide (II), which was probably reduced during the time-on-stream, in favor of a shorter Ni-O bond, which could correspond to Ni-O in $NiAl_2O_4$ ternary oxide or $Ni(OH)_2$ in which the Ni-O bond is found ca. 1.97 Å [68].

Table 6. CNs, Radial Distance (R), Debye−Waller Factor (σ), and R-Factor Determined by EXAFS fitting of the Ni K-Edge of the post-run mixed-oxide catalyst promoted with cobalt

NiCo-S				
Path	**CN**	**R (Å)**	**σ^2 (Å^2)**	**R-factor (10^{-2})**
Ni-Me*	11.1 ± 0.7	2.479 ± 0.02	0.0075 ± 0.0006	0.7
Ni-O	0.4 ± 0.1	2.055 ± 0.02	0.0045 ± 0.0005	
NiCo-D				
Path	**CN**	**R (Å)**	**σ^2 (Å^2)**	**R-factor (10^{-2})**
Ni-Me*	10.1± 0.9	2.487 ± 0.01	0.0074 ± 0.0007	0.8
Ni-O	0.5 ± 0.2	1.991 ± 0.03	0.0021± 0.0005	
CoNi-D				
Path	**CN**	**R (Å)**	**σ^2 (Å^2)**	**R-factor (10^{-2})**
Ni-Me*	8.4 ± 0.7	2.488 ± 0.01	0.0071 ± 0.0007	0.8
Ni-O	0.8 ± 0.2	2.036 ± 0.02	0.0029 ± 0.0005	

* where Me is Ni or Co

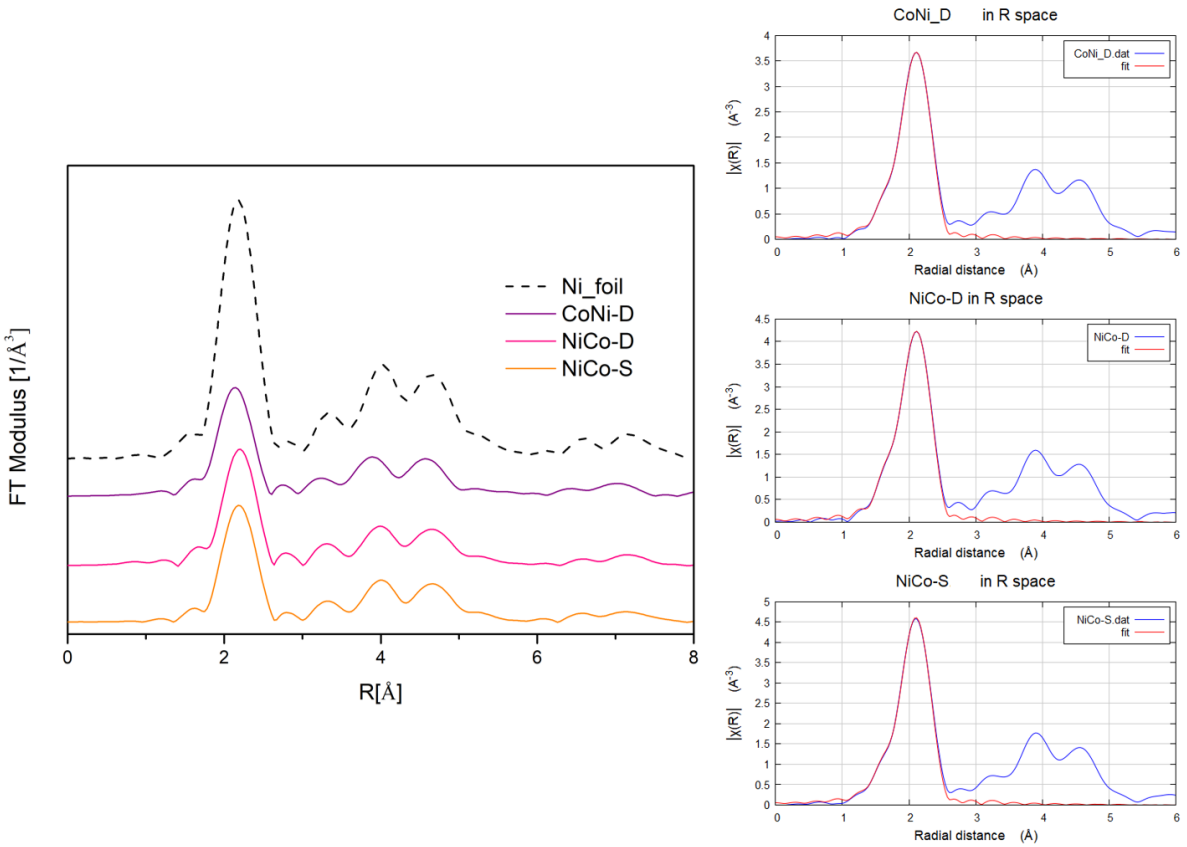

Figure 15. EXAFS for the post-run catalysts

6. Conclusions

Solution combustion synthesis can be an efficient method for the preparation of multielemental catalysts if the promoter (cobalt in this case) is introduced separately from the active phase. The use of two-step synthesis led to the formation of a material with increased availability of both the active material and promoter, which improved the development of the surface medium-strength and strong basicity. This led to improvement of the catalytic performance in CO_2 methanation. Additionally, the introduction of nickel separately from cobalt led to a material with enhanced reducibility, compared to the catalyst obtained by one-step synthesis. In all studied samples, nickel formed an alloy with cobalt. The simultaneous combustion of all the precursors (NiCo-S catalyst) led to the dissociation of both Ni and Co to the Mg-Al oxide matrix and a further formation of catalytically inactive $NiAl_2O_4$ and $CoAl_2O_4$. All of the reported

strategies led to the formation of relatively large nickel crystallites, especially for the sample prepared by one-step synthesis.

Acknowledgments

Paulina Summa would like to acknowledge the French Embassy in Poland for providing the BGF Doctorate Cotutelle scholarship. Katarzyna Świrk is MSCA-IF researcher at the Norwegian University of Science and Technology in Norway. This project has received funding from the European Union's Horizon 2020 research and innovation program under the Marie Skłodowska-Curie grant agreement No 892571.

The project team at SNBL is acknowledged for experimental assistance (SNBL-BM31).

References

[1] IPCC, Climate Change 2021 The Physical Science Basis Summary for Policymakers Working Group I Contribution to the Sixth Assessment Report of the Intergovernmental Panel on Climate Change, 2021.

[2] European Commission, 2050 Long-Term Strategy | Δράση Για Το Κλίμα, (2018).

[3] I. Kuznecova, J. Gusca, Property based ranking of CO and CO2 methanation catalysts, Energy Procedia. 128 (2017) 255–260. doi:10.1016/j.egypro.2017.09.068.

[4] W. Wang, J. Gong, Methanation of carbon dioxide: An overview, Front. Chem. Eng. China. 5 (2011) 2–10. doi:10.1007/s11705-010-0528-3.

[5] G.A. Mills, F.W. Steffgen, Catalytic methanation, Catal. Rev. 8 (1974) 159–210. doi:10.1080/01614947408071860.

[6] A. Trovarelli, G. Dolcetti, C. de Leitenburg, J. Kaspar, CO2 Hydrogenation Over Platinum Group Metals Supported on CeO2: Evidence for a Transient Metal-Support Interaction, Stud. Surf. Sci. Catal. 75 (1993) 2781–2784. doi:10.1016/S0167-2991(08)64404-3.

[7] R. Thalinger, T. Götsch, C. Zhuo, W. Hetaba, W. Wallisch, M. Stöger-Pollach, D. Schmidmair, B. Klötzer, S. Penner, Rhodium-Catalyzed Methanation and Methane Steam Reforming Reactions on Rhodium–Perovskite Systems: Metal–Support Interaction, ChemCatChem. 8 (2016) 2057–2067. doi:10.1002/cctc.201600262.

[8] J.A. Martins, A.C. Faria, M.A. Soria, C. V. Miguel, A.E. Rodrigues, L.M. Madeira, Co2 methanation over hydrotalcite-derived nickel/ruthenium and supported ruthenium catalysts, Catalysts. 9 (2019) 1008. doi:10.3390/catal9121008.

[9] Z. Boukha, C. Jiménez-González, M. Gil-Calvo, B. de Rivas, J.R. González-Velasco, J.I. Gutiérrez-Ortiz, R. López-Fonseca, MgO/NiAl2O4 as a new formulation of reforming catalysts: Tuning the surface properties for the enhanced partial oxidation of methane, Appl. Catal. B Environ. 199 (2016) 372–383. doi:10.1016/j.apcatb.2016.06.045.

[10] L. Zhou, L. Li, N. Wei, J. Li, J.-M. Basset, Effect of NiAl2O4 Formation on Ni/Al2O3 Stability during Dry Reforming of Methane, ChemCatChem. 7 (2015) 2508–2516. doi:https://doi.org/10.1002/cctc.201500379.

[11] P. Summa, K. Świrk, Y. Wang, B. Samojeden, M. Rønning, C. Hu, M. Motak, P. Da Costa, Effect of cobalt promotion on hydrotalcite-derived nickel catalyst for CO2 methanation, Appl. Mater. Today. 25 (2021) 101211. doi:10.1016/j.apmt.2021.101211.

[12] K. Świrk, P. Summa, D. Wierzbicki, M. Motak, P. Da Costa, Vanadium promoted Ni(Mg,Al)O hydrotalcite-derived catalysts for CO2 methanation, Int. J. Hydrogen Energy. (2021). doi:https://doi.org/10.1016/j.ijhydene.2021.02.172.

[13] P.H. Ho, G.S. de Luna, S. Angelucci, A. Canciani, W. Jones, D. Decarolis, F. Ospitali, E.R. Aguado, E. Rodríguez-Castellón, G. Fornasari, A. Vaccari, A.M. Beale, P. Benito, Understanding structure-activity relationships in highly active La promoted Ni catalysts for CO2 methanation, Appl. Catal. B Environ. 278 (2020) 119256. doi:10.1016/j.apcatb.2020.119256.

[14] P. Shafiee, S.M. Alavi, M. Rezaei, Mechanochemical synthesis method for the preparation of mesoporous Ni–Al2O3 catalysts for hydrogen purification via CO2 methanation, J. Energy Inst. 96 (2021) 1–10. doi:10.1016/j.joei.2021.01.015.

[15] P. Summa, B. Samojeden, M. Motak, Dry and steam reforming of methane. Comparison and analysis of recently investigated catalytic materials. A short review, Polish J. Chem. Technol. 21 (2019) 31–37. doi:10.2478/pjct-2019-0017.

[16] K. Świrk, H. Zhang, S. Li, Y. Chen, M. Rønning, M. Motak, T. Grzybek, P. Da Costa, Carbon-resistant NiO-Y2O3-nanostructured catalysts derived from double-layered hydroxides for dry reforming of methane, Catal. Today. (2020). doi:10.1016/j.cattod.2020.03.032.

[17] P. Summa, B. Samojeden, M. Motak, D. Wierzbicki, I. Alxneit, K. Świerczek, P. Da Costa, Investigation of Cu promotion effect on hydrotalcite-based nickel catalyst for CO2 methanation, Catal. Today. 384–386 (2022) 133–145. doi:10.1016/j.cattod.2021.05.004.

[18] P. Summa, K. Świrk, D. Wierzbicki, M. Motak, I. Alxneit, M. Rønning, P. Da Costa, Co-Precipitated Ni-Mg-Al Hydrotalcite-Derived Catalyst Promoted with Vanadium for

CO2 Methanation, Molecules. 26 (2021). doi:10.3390/molecules26216506.

[19] N. Dewangan, W.M. Hui, S. Jayaprakash, A.-R. Bawah, A.J. Poerjoto, T. Jie, A. Jangam, K. Hidajat, S. Kawi, Recent Progress on Layered Double Hydroxide (LDH) Derived Metal-Based Catalysts for CO2 Conversion to Valuable Chemicals, Catal. Today. (2020). doi:10.1016/j.cattod.2020.06.020.

[20] G. Giorgianni, C. Mebrahtu, M.E. Schuster, A.I. Large, G. Held, P. Ferrer, F. Venturini, D. Grinter, R. Palkovits, S. Perathoner, G. Centi, S. Abate, R. Arrigo, Elucidating the mechanism of the CO2methanation reaction over Ni-Fe hydrotalcite-derived catalysts: Via surface-sensitive in situ XPS and NEXAFS, Phys. Chem. Chem. Phys. 22 (2020) 18788–18797. doi:10.1039/d0cp00622j.

[21] A. Boffa, C. Lin, A.T. Bell, G.A. Somorjai, Promotion of CO and CO2 hydrogenation over Rh by metal oxides: The influence of oxide lewis acidity and reducibility, J. Catal. 149 (1994) 149–158. doi:10.1006/jcat.1994.1280.

[22] S. Ma, Y. Tan, Y. Han, Methanation of syngas over coral reef-like Ni/Al2O3 catalysts, J. Nat. Gas Chem. 20 (2011) 435–440. doi:10.1016/S1003-9953(10)60192-2.

[23] C. Liang, H. Tian, G. Gao, S. Zhang, Q. Liu, D. Dong, X. Hu, Methanation of CO2 over alumina supported nickel or cobalt catalysts: Effects of the coordination between metal and support on formation of the reaction intermediates, Int. J. Hydrogen Energy. 45 (2020) 531–543. doi:10.1016/j.ijhydene.2019.10.195.

[24] O. Bergadà, P. Salagre, Y. Cesteros, F. Medina, J.E. Sueiras, Adsorption of carbon dioxide in several aged hydrotalcites and calcined hydrotalcites: Influence of microwave irradiation during the ageing step on their basic properties, Adsorpt. Sci. Technol. 25 (2007) 143–154. doi:10.1260/026361707782398191.

[25] J.I. Di Cosimo, C.R. Apesteguía, M.J.L. Ginés, E. Iglesia, Structural requirements and reaction pathways in condensation reactions of alcohols on MgyAlOx catalysts, J. Catal. 190 (2000) 261–275. doi:10.1006/jcat.1999.2734.

[26] B. Seo, E.H. Ko, J. Boo, M. Kim, D. Kang, N.-K. Park, CO2 Hydrogenation on NixMg1−xAl2O4: A Comparative Study of MgAl2O4 and NiAl2O4, Catalysts. 11 (2021). doi:10.3390/catal11091026.

[27] L. Ji, J. Lin, H.C. Zeng, Metal-Support Interactions in Co/Al2O3 Catalysts: A Comparative Study on Reactivity of Support, J. Phys. Chem. B. 104 (2000) 1783–1790. doi:10.1021/jp993400l.

[28] J. Horlyck, M. Sara, E.C. Lovell, R. Amal, J. Scott, Effect of Metal-Support Interactions in Mixed Co/Al Catalysts for Dry Reforming of Methane, ChemCatChem. 11 (2019) 3432–3440. doi:10.1002/cctc.201900638.

[29] P. Shafiee, S.M. Alavi, M. Rezaei, Solid-state synthesis method for the preparation of cobalt doped Ni–Al2O3 mesoporous catalysts for CO2 methanation, Int. J. Hydrogen Energy. (2020). doi:10.1016/j.ijhydene.2020.10.221.

[30] P. Shafiee, S.M. Alavi, M. Rezaei, F. Jokar, Promoted Ni–Co–Al2O3 nanostructured catalysts for CO2 methanation, Int. J. Hydrogen Energy. 47 (2022) 2399–2411. doi:10.1016/j.ijhydene.2021.10.197.

[31] B. Alrafei, I. Polaert, A. Ledoux, F. Azzolina-Jury, Remarkably stable and efficient Ni and Ni-Co catalysts for CO2 methanation, Catal. Today. 346 (2020) 23–33. doi:10.1016/j.cattod.2019.03.026.

[32] L. Xu, X. Lian, M. Chen, Y. Cui, F. Wang, W. Li, B. Huang, CO2 methanation over Co–Ni bimetal-doped ordered mesoporous Al2O3 catalysts with enhanced low-

temperature activities, Int. J. Hydrogen Energy. 43 (2018) 17172–17184. doi:10.1016/j.ijhydene.2018.07.106.

[33] Q. Liu, B. Bian, J. Fan, J. Yang, Cobalt doped Ni based ordered mesoporous catalysts for CO2 methanation with enhanced catalytic performance, Int. J. Hydrogen Energy. 43 (2018) 4893–4901. doi:10.1016/j.ijhydene.2018.01.132.

[34] O.H. Ojeda-Niño, F. Gracia, C. Daza, Role of Pr on Ni−Mg−Al Mixed Oxides Synthesized by Microwave- Assisted Self-Combustion for Dry Reforming of Methane, Ind. Eng. Chem. Res. 58 (2019) 7909–7921. doi:10.1021/acs.iecr.9b00557.

[35] F. Cavani, F. Trifiro, A. Vaccari, Hydrotalcite-type anionic clays: preparation, properties and applications, I I (I99 I) 173-301 Elsevier Science Publishers, Catal. Today. 11 (1991) 173–301.

[36] P. Summa, M. Gajewska, L. Li, C. Hu, B. Samojeden, M. Motak, P. Da Costa, Solution combustion synthesis as an alternative synthesis route for novel Ni-Mg-Al mixed-oxide catalyst for CO2 methanation, J. CO2 Util. 60 (2022) 101983. doi:https://doi.org/10.1016/j.jcou.2022.101983.

[37] Y. Jiang, T. Huang, L. Dong, Z. Qin, H. Ji, Ni/bentonite catalysts prepared by solution combustion method for CO2 methanation, Chinese J. Chem. Eng. (2018) 2361–2367. doi:10.1016/j.cjche.2018.03.029.

[38] A. Varma, A.S. Mukasyan, A.S. Rogachev, K. V. Manukyan, Solution Combustion Synthesis of Nanoscale Materials, Chem. Rev. 116 (2016) 14493–14586. doi:10.1021/acs.chemrev.6b00279.

[39] S.L. González-Cortés, F.E. Imbert, Fundamentals, properties and applications of solid catalysts prepared by solution combustion synthesis (SCS), Appl. Catal. A Gen. 452

(2013) 117–131. doi:10.1016/j.apcata.2012.11.024.

[40] A. Tsoukalou, P.M. Abdala, D. Stoian, X. Huang, M.G. Willinger, A. Fedorov, C.R. Müller, Structural Evolution and Dynamics of an In2O3 Catalyst for CO2 Hydrogenation to Methanol: An Operando XAS-XRD and in Situ TEM Study, J. Am. Chem. Soc. 141 (2019) 13497–13505. doi:10.1021/jacs.9b04873.

[41] J.A. Dumesic, G.W. Huber, M. Boudart, Principles of Heterogeneous Catalysis, in: Handb. Heterog. Catal., American Cancer Society, 2008. doi:https://doi.org/10.1002/9783527610044.hetcat0001.

[42] K. Liu, N. Zakharova, A. Adeyilola, L. Zeng, Experimental Study on the Pore Shape Damage of Shale Samples during the Crushing Process, Energy and Fuels. 35 (2021) 2183–2191. doi:10.1021/acs.energyfuels.0c03297.

[43] S. Sun, L. Feng, L. Tang, J. Wu, C. Ma, Microstructural investigation of gas shale in Longmaxi Formation, Lower Silurian, NE Sichuan Basin, China, Energy Explor. Exploit. 35 (2017) 406–429. doi:10.1177/0144598716684304.

[44] J.C. Toniolo, A.S. Takimi, C.P. Bergmann, Nanostructured cobalt oxides (Co3O4 and CoO) and metallic Co powders synthesized by the solution combustion method, Mater. Res. Bull. 45 (2010) 672–676. doi:10.1016/j.materresbull.2010.03.001.

[45] S.T. Aruna, A.S. Mukasyan, Combustion synthesis and nanomaterials, Curr. Opin. Solid State Mater. Sci. 12 (2008) 44–50. doi:10.1016/j.cossms.2008.12.002.

[46] A.U. Chavan, J.H. Kim, H.N. Im, S.J. Song, Role of different oxide to fuel ratios in solution combustion synthesis of SnO2 nanoparticles, J. Korean Ceram. Soc. 53 (2016) 122–127. doi:10.4191/kcers.2016.53.1.122.

[47] J. Bai, F. Meng, C. Wei, Y. Zhao, H. Tan, J. Liu, Solution combustion synthesis and

characteristics of nanoscale MgO powders, Ceram. - Silikaty. 55 (2011) 20–25.

[48] K. V. Manukyan, Solution Combustion Synthesis of Catalysts, Concise Encycl. Self-Propagating High-Temperature Synth. (2017) 347–348. doi:10.1016/b978-0-12-804173-4.00137-x.

[49] P. Dinka, A.S. Mukasyan, In situ preparation of oxide-based supported catalysts by solution combustion synthesis, J. Phys. Chem. B. 109 (2005) 21627–21633. doi:10.1021/jp054486n.

[50] D. Wierzbicki, R. Baran, R. Dębek, M. Motak, T. Grzybek, M.E. Gálvez, P. Da Costa, The influence of nickel content on the performance of hydrotalcite-derived catalysts in CO2 methanation reaction, Int. J. Hydrogen Energy. 42 (2017) 23548–23555. doi:10.1016/j.ijhydene.2017.02.148.

[51] K. Świrk, M.E. Gálvez, M. Motak, T. Grzybek, M. Rønning, P. Da Costa, Yttrium promoted Ni-based double-layered hydroxides for dry methane reforming, J. CO2 Util. (2018). doi:10.1016/j.jcou.2018.08.004.

[52] J. Sun, A. Gao, X. Wang, X. Xu, J. Song, Removal of Phosphorus from Wastewater by Different Morphological Alumina, Molecules. 25 (2020). doi:10.3390/molecules25133092.

[53] W. Chu, W. Yang, L. Lin, Selective oxidation of methane to syngas over NiO/barium hexaaluminate, Catal. Letters. 74 (2001) 139–144. doi:10.1023/A:1016622301743.

[54] J. Liu, C. Li, F. Wang, S. He, H. Chen, Y. Zhao, M. Wei, D.G. Evans, X. Duan, Enhanced low-temperature activity of CO2 methanation over highly-dispersed Ni/TiO2 catalyst, Catal. Sci. Technol. 3 (2013) 2627–2633. doi:10.1039/c3cy00355h.

[55] N.A.A. Fatah, A.A. Jalil, N.F.M. Salleh, M.Y.S. Hamid, Z.H. Hassan, M.G.M.

Nawawi, Elucidation of cobalt disturbance on Ni/Al2O3 in dissociating hydrogen towards improved CO2 methanation and optimization by response surface methodology (RSM), Int. J. Hydrogen Energy. 45 (2020) 18562–18573. doi:10.1016/j.ijhydene.2019.04.119.

[56] I. Alxneit, Particle Size Distributions from Electron Microscopy Images: Avoiding Pitfalls, J. Phys. Chem. A. 124 (2020) 10075–10081. doi:10.1021/acs.jpca.0c07840.

[57] M. Akri, S. Zhao, X. Li, K. Zang, A.F. Lee, M.A. Isaacs, W. Xi, Y. Gangarajula, J. Luo, Y. Ren, Y.T. Cui, L. Li, Y. Su, X. Pan, W. Wen, Y. Pan, K. Wilson, L. Li, B. Qiao, H. Ishii, Y.F. Liao, A. Wang, X. Wang, T. Zhang, Atomically dispersed nickel as coke-resistant active sites for methane dry reforming, Nat. Commun. 10 (2019) 1–10. doi:10.1038/s41467-019-12843-w.

[58] T.S. Galhardo, A.H. Braga, B.H. Arpini, J. Szanyi, R. V Gonçalves, B.F. Zornio, C.R. Miranda, L.M. Rossi, Optimizing Active Sites for High CO Selectivity during CO2 Hydrogenation over Supported Nickel Catalysts, J. Am. Chem. Soc. 143 (2021) 4268–4280. doi:10.1021/jacs.0c12689.

[59] N. Evdokimenko, Z. Yermekova, S. Roslyakov, O. Tkachenko, G. Kapustin, D. Bindiug, A. Kustov, A.S. Mukasyan, Sponge-like CoNi Catalysts Synthesized by Combustion of Reactive Solutions : Stability and Performance for, (2022).

[60] A. Wang, H. Yin, M. Ren, H. Lu, J. Xue, T. Jiang, Preparation of nickel nanoparticles with different sizes and structures and catalytic activity in the hydrogenation of p-nitrophenol, New J. Chem. - NEW J CHEM. 34 (2010). doi:10.1039/b9nj00657e.

[61] S. Golden, Z. Nazarpoor, M. Launois, R.-F. Liu, P.S. Maram, Development of Non-Copper Advanced Spinel Mixed Metal Oxides for Zero-Precious Metal and Ultra-Low Precious Metal Next-Generation TWC, in: 2016. doi:10.4271/2016-01-0933.

[62] W. Carrillo-Cabrera, D.J. Smith, Hrtem study of the surface and bulk of nickel oxide: Influence of annealing and quenching, Solid State Ionics. 32–33 (1989) 749–758. doi:https://doi.org/10.1016/0167-2738(89)90354-8.

[63] C. Li, S. Liu, Preparation and Characterization of Ni (OH) 2 and NiOMesoporous Nanosheets, in: 2014.

[64] G. Xu, D. Yu, D. Zheng, S. Wang, W. Xue, X.E. Cao, H. Zeng, X. Xiao, M. Ge, W.K. Lee, M. Zhu, Fast Heat Transport Inside Lithium-Sulfur Batteries Promotes Their Safety and Electrochemical Performance, IScience. 23 (2020). doi:10.1016/j.isci.2020.101576.

[65] J. López-Tinoco, R. Mendoza-Cruz, L. Bazán-Díaz, S.C. Karuturi, M. Martinelli, D.C. Cronauer, A.J. Kropf, C.L. Marshall, G. Jacobs, The preparation and characterization of co–ni nanoparticles and the testing of a heterogenized co–ni/alumina catalyst for co hydrogenation, Catalysts. 10 (2020). doi:10.3390/catal10010018.

[66] A.I. Frenkel, A. Yevick, C. Cooper, R. Vasic, Modeling the Structure and Composition of Nanoparticles by Extended X-Ray Absorption Fine-Structure Spectroscopy, Annu. Rev. Anal. Chem. 4 (2011) 23–39. doi:10.1146/annurev-anchem-061010-113906.

[67] A. Jentys, Estimation of mean size and shape of small metal particles by EXAFS, Phys. Chem. Chem. Phys. 1 (1999) 4059–4063. doi:10.1039/A904654B.

[68] M. Bustamante, I. Valencia, M. Castro, Theoretical study of [Ni (H2O)n]2+(H2O)m (n ≤ 6, m ≤ 18)., J. Phys. Chem. A. 115 17 (2011) 4115–4134.